THE UNIVERSITY OF CHICAGO

HYBRID, MULTIDIMENSIONAL MAGNETIC RESONANCE IMAGING OF PROSTATE CANCER

A DISSERTATION SUBMITTED TO

THE FACULTY OF THE DIVISION OF THE BIOLOGICAL SCIENCES

AND THE PRITZKER SCHOOL OF MEDICINE

IN CANDIDACY FOR THE DEGREE OF

DOCTOR OF PHILOSOPHY

COMMITTEE ON MEDICAL PHYSICS

BY

MEREDITH SADINSKI

CHICAGO, ILLINOIS

JUNE 2016

“*Are you graduating yet?”*

–Xiaobing Fan, 2014, 2015, 2016…

TABLE OF CONTENTS

LIST OF FIGURES

LIST OF TABLES

ACKNOWLEDGEMENTS

I'd like to thank my advisors, Greg and Aytek. Greg, I could not have done it without you. Seriously, they said I absolutely needed an advisor. You have been an invaluable mentor and role model for being a successful and impactful researcher. I appreciate your support and your sagacity and I look forward to future collaborations. Aytek, I have learned so much from you. You have always been willing and enthusiastic to answer any question I have and have imparted to me the importance of making sure research is relevant and useful. I would also like to thank my committee, Milica, Yulei and Steffen, for all of their guidance and input.

Thank you to all of the technologists I have worked with; Bruce and Stan, who have not only taken the time to teach me to scan and answer any question I have but also have provided invaluable moments of comedic relief in Q-300. Donna, Deanna, Felicia, Erica, Jean, Renu, Dana, Holly, Joanne and Ali: I always look forward to working with you in DCAM. I leave with smile on my face every time. Felicia, I'll see you at Dallas BBQ.

To Sharon, my work mom: I'll miss having you around as a confidant. Thanks for all the advice and support (and of course movie recommendations). To Jim, thanks for letting me tag along on animal experiments and, more importantly, for the fly tying advice and materials! Keep an eye out for me on the Green; I'll be the one in the red raft with the monster trout!

Thank you to Tom Miller, my junior high science teacher and basketball coach who gave me the copy of *Stephen Hawking's Universe* that first piqued my interest in physics and continued to encourage me with reading material and engaging discussions. Here I am, 14 years later, receiving my doctorate.

Thank you to my parents who have encouraged me to pursue my interests and fostered my insatiable curiosity. You have taken me to every public lecture and young scientist event I wanted to go to. To my sister, Cassie: although I may look down on you now I'll always look up to you as a role model. I may not have liked always being "Cassie's little sister" growing up but it was definitely a good reputation to start out with. To my grandfather, Buck Sample: since I was little, sitting on your lap and eating ramen together, I've always been so proud to be your granddaughter. You have led such an incredible, adventure-filled life and you continue to inspire me every day.

To Dave: I'm so excited to get my degree beside you and embark on new adventures together in New York. You've been there, supporting me, through the good times and the tough times. I never thought I would meet someone as silly as me, especially not in graduate school. If you are my local maximum, you sure are a strong local maximum!

Finally, to the faculty and students of the GPMP, thank you for the mentorship and friendship. The kindness and attitude of the GPMP continues to impress me and has made the last five years grueling but fun!

ABSTRACT

Prostate cancer is the most commonly diagnosed cancer among men, estimated to affect one in six American men. Despite its high prevalence, nearly 50% of prostate cancer is insignificant and unrelated to cause of death of the patient. It is thus of paramount importance that physicians are able to make informed decisions on course of treatment for prostate cancer patients; an aggressive treatment option such as radiation therapy or surgery with risk of adverse side effects is necessary for high grade cancers while active surveillance may be sufficient for lower grade cancers. Current methods for assessing the aggressiveness of prostate cancer are insufficient and repeat biopsies or histological analysis of prostatectomy specimens often show disagreement with initial staging. MRI has become a useful, non-invasive tool for prostate cancer screening. A clinical multiparametric MRI (mp-MRI) exam typically includes T1, T2 and apparent diffusion coefficient (ADC) maps, extracted from T1-weighted, T2-weighted and diffusion-weighted MRI (DWI) sequences, respectively. However, the efficacy of PCa MRI is limited by the inability to distinguish the signal from cancerous foci from the background signal from normal tissue using standard, clinical MRI sequences.

This dissertation investigates a hybrid, multidimensional imaging approach to prostate MRI, which looks at how standard measures (ADC, T1, T2) react to changes in sequence parameters (TE, TR, b). This enables a selective filtration of particular tissue components and subsequent emphasis of differences in tissue structure indicative of prostate cancer. My results suggest that using hybrid imaging to identify differences in tissue structure could lead to better differentiation between normal tissue, aggressive

prostate cancer and benign tumors or conditions. Hybrid imaging provides structural information undetectable using conventional mp-MRI. It may therefore provide independent, diagnostic information that compliments ADC, T1 or T2 values and increase diagnostic accuracy when used in combination with conventional mp-MRI. Structural markers such as decreased luminal volume, increased cellularity, and nucleomegaly become more prominent with increased Gleason Score. Hybrid MRI may therefore be useful for noninvasively determining Gleason Score in the future.

CHAPTER 1

INTRODUCTION

1.1 Prostate Cancer

Since the first case was described in 1853, prostate cancer has become a prominent public health concern. In that initial description, prostate cancer was described as "a very rare disease" (1). The National Cancer Institute estimates that nearly one in six American men will develop prostate cancer during his lifetime with an estimated 220,800 new diagnoses that were predicted for 2015. This makes prostate cancer the most common non-cutaneous cancer among males and the second most common cancer overall, comprising an estimated 13.3% of newly diagnosed cancers in 2015 (2).

Despite the high prevalence of prostate cancer, most are insignificant and unrelated to the death of the patient. An estimated 2,795,592 men were living with prostate cancer in the United States in 2012. Despite comprising 13.3% of new cancer diagnoses, prostate cancer was only responsible for an estimated 4.7% of all cancer deaths in 2015. Autopsy studies have shown that between 30 and 80 percent of men who died of other causes had latent prostate carcinoma, with the percentage depending on age (3). Thus, it’s extremely important that methods exist which can distinguish aggressive, rapidly growing prostate cancer from indolent disease and normal, benign tissue.

The normal prostate is composed of fluid-filled ducts surrounded by fibrous, muscular tissue consisting of stromal cells (figure 1.1). Branching acini at the end of ducts

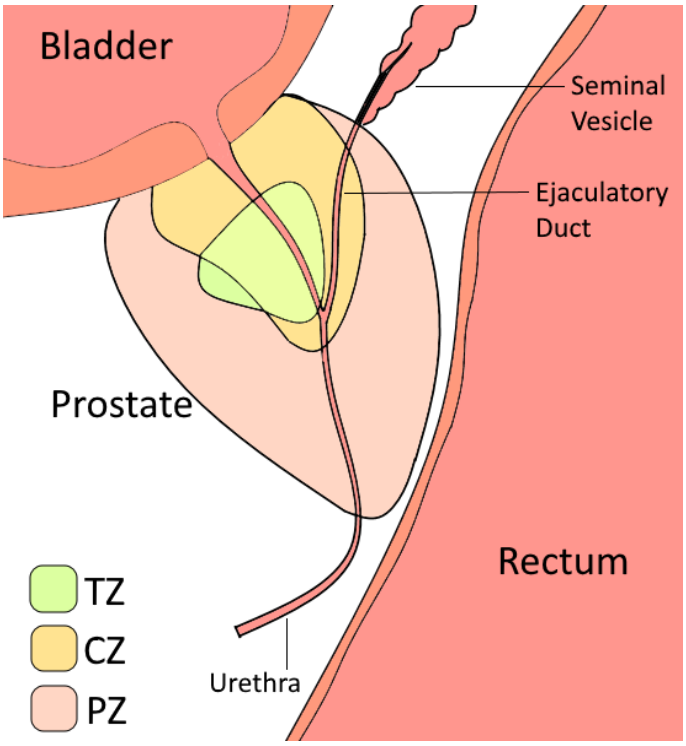

Figure 1.1 An anatomical diagram of the prostate. Approximately the size of a walnut, the prostate is located between the bladder and the rectum. It is conical in shape with the base superior and the apex inferior. The central portion is the fibrous Transition Zone (TZ) surrounded by the Central Zone (CZ). The TZ enlarges with age so that the CZ is only apparent in young men. The urethra runs through the TZ. The Peripheral Zone (PZ) surrounds the TZ/CZ on three sides and contains the majority of glandular tissue. The majority of prostate cancers are adenocarcinomas in the PZ.

are surrounded by a layer of epithelial cells. Prostate cancer occurs when these epithelial cells proliferate abnormally outward into the surrounding stromal environment and inward into the lumen of the ducts. The cancer aggressiveness is categorized by the Gleason grading system.

The Gleason grading system was developed in the 1960s, and modified in 2005, to evaluate prostate cancer prognosis based on architectural features as seen on histology (4,5). There are five histologic Gleason patterns with distinct characteristics:

Grade 1: *Circumscribed nodule of closely packed, but separate, uniform, rounded to oval, medium-sized acini (larger glands than pattern 3)*

Grade 2: *Like pattern 1, fairly circumscribed, but at the edge of the tumor nodule, there may be minimal infiltration; glands are more loosely arranged and not quite as uniform as Gleason pattern 1*

Grade 3: *Discrete glandular units: typically, smaller glands than seen in Gleason patterns 1 or 2; infiltrates in and among nonneoplastic prostate acini; marked variation in size and shape; smoothly circumscribed, small, cribriform nodules of tumor*

Grade 4: *Fused microacinar glands: ill-defined glands with poorly formed glandular lumina; large, cribriform glands; cribriform glands with an irregular border; hypernephromatoid*

Grade 5: *Essentially no glandular differentiation, composed of solid sheets, cords, or single cells; comedocarcinoma with central necrosis surrounded by papillary, cribriform, or solid masses*

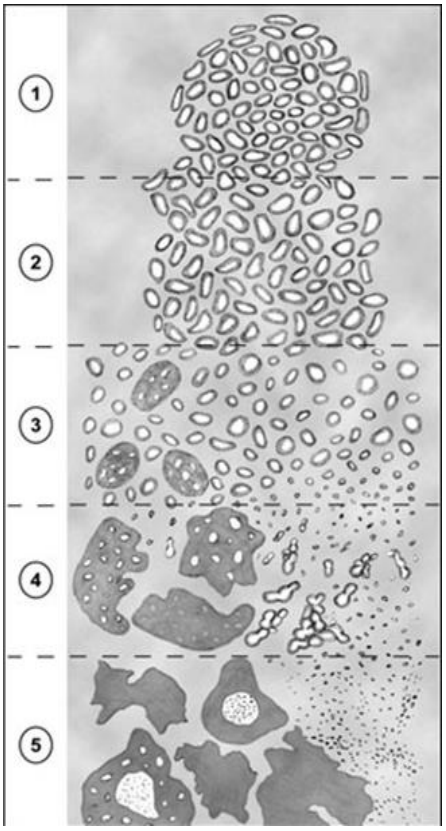

Figure 1.2 Modified Gleason grading system diagram showing the 5 Gleason patterns (5).

A Gleason score is assigned to a tumor by adding the primary grade (comprising greater than 50% of tumor sample volume) and secondary grade (comprising less than

50%, but greater than 5% of tumor volume). Increasingly, a tertiary grade (third most prevalent) may be denoted, particularly if it is high.

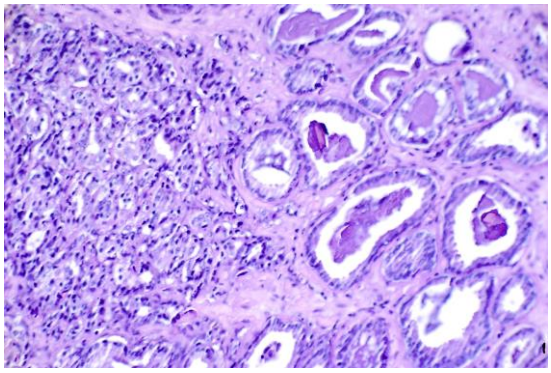

Figure 1.3 Prostate histology. Low grade (Gleason 3) glandular tissue is seen on the right. Higher grade, cancerous tissue (Gleason 4) is seen on the left. Note the larger number and volume of acini on the right compared to the dense cellular growth on the left (image courtesy of the National Institute of Health, photographer: Otis Brawley).

Patient prognosis is highly correlated with Gleason score. Gleason scores 2-5 are not generally reported. Gleason 6 tumors have a very favorable prognosis. A study of 7869 men who underwent radical prostatectomy between 2004 and 2011 found that the rate of biochemical recurrence-free survival (BRFS, defined as postoperative PSA level less than 0.2 ng/ml) at 5 years for men with Gleason Score ≤6 was 94.6% based on biopsy and 96.6% based on radical prostatectomy. Although this category included Gleason scores 4-6, 99.8% of the tumors were Gleason 6. Gleason 3+4=7 tumors also had a good prognosis with 82.7% biopsy-based and 88.1% radical prostatectomy-based 5-year BRFS. Gleason 4+3=7 tumors showed 65.1% biopsy-based and 69.7% radical prostatectomy-based 5-year BRFS. The prognosis of these tumors was more similar to Gleason 8 tumors, for which the biopsy-based and radical prostatectomy-based 5-year BRFS was 63.1% and 63.7%, respectively. The prognosis for Gleason 9-10 tumors is poor, with both biopsy-based and prostatectomy-based 5-year BRFS of 34.5% (6). Studies have also reported that the presence of Gleason

pattern 5 is the greatest prognostic predictor for death from prostate cancer following radiation therapy and hormonal therapy. (7)

1.2 Detection and Diagnosis

1.2.1 Screening

Given the high incidence of prostate cancer, screening is generally recommended. Current screening techniques, however, are inaccurate. The American Urological Association recommends that men over age 50 with a life expectancy of greater than 10 years get a prostate cancer screening every one to three years (8). This increases to every year over the age of 40 for men with a family history of aggressive prostate cancer and African American men, who statistically have a greater risk of developing prostate cancer. Such a screening typically consists of a digital rectal exam (DRE) in conjunction with Prostate Specific Antigen (PSA) testing.

Digital rectal exams detect enlargement of the prostate or changes in texture that may be indicative of prostate cancer. Inexpensive, fast, and relatively non-invasive, these exams are a valuable component of regular prostate cancer screening. However, digital rectal exams alone have been shown to have a low sensitivity and be only moderately reproducible (9,10). Additionally, the test is only able to detect irregularities in the section of the prostate proximal to the rectum. When combined with PSA testing, the sensitivity and specificity of digital rectal exams improves (11).

PSA is a glycoprotein generated by the luminal epithelial cells lining the prostatic ducts. It is produced by both malignant and benign glandular tissue, most of which is in

the peripheral zone. The PSA gene is regulated by Androgen receptors. Most PSA is excreted into the seminal fluid where it liquefies the fluid, allowing increased motility of the spermatozoa. The PSA, along with the seminal fluid, enters the excretory ducts and then the urethra. A very small amount, however, ends up in the blood. In normal prostate tissue, the ordered glandular architecture confines the PSA to the prostate. With prostate cancer, this architecture is disrupted and PSA levels in the serum are about 10 times higher per gram of tissue than in benign hyperplasia. However, there is also a great deal of variation in serum PSA levels. Biological sources of variation include PSA production levels and renal elimination. Additionally, analytic variation sources include assay choice and processing differences during PSA testing. A common cut-off limit for serum PSA to be considered high is 4.0 ng/mL, but there is no range of normal versus abnormal PSA levels. In fact, the Prostate Cancer Prevention Trial showed prostate cancer in 15.2% of 2950 men aged 62-91 with PSA less than 4 and normal DRE (14.9 % of all cancers were GS 7+) (12).

PSA production also increases due to prostate or perineal trauma, ejaculation, prostate infection, urine retention, prostate inflammation and benign prostatic hyperplasia (BPH). BPH, not cancer, is the most common cause of elevated PSA levels. Other PSA-based metrics including free PSA, PSA density, PSA slope and PSA doubling time have become more commonplace in an attempt to improve specificity.

The benefit of prostate cancer screening is still widely debated. Multiple European countries and all Scandinavian countries have declined to institute prostate cancer screening guidelines due to a "lack of direct evidence" of its efficacy (13). The accuracy of PSA testing has been largely debunked in recent years. A 2012 European

Randomized Study of Screening for Prostate Cancer published in *the New England Journal of Medicine* found that PSA screening gave a relative reduction in the risk of death due to prostate cancer of 29% compared with no screening over an 11 year follow-up. However, the absolute reduction in mortality was exceedingly low. To prevent a single death from prostate cancer at 11 years of follow-up, 1055 men need to be encouraged to undergo screening and 37 cancers would need to be detected (14). This and similar studies led the U.S. Preventative Services Task Force Recommendation Statement, published in 2012, to recommend against PSA screening. The statement stated, “There is moderate certainty that the benefits of PSA-based screening for prostate cancer do not outweigh the harms.” The “harms” noted include a 10-12% false-positive rate and 5% treatment complication rate out of all men screened (15).

The low specificity of screening has led to a large over-detection rate, reported anywhere from 16 to 56% (16-18). This results in a large number of unnecessary biopsies, which are both painful and inconvenient for the patient and taxing on the healthcare system.

1.2.2 Biopsy

Patients for whom DRE or PSA screening detects any abnormality are referred for a prostate biopsy. Prostate biopsies are typically transrectal ultrasound (TRUS) guided. The procedure involves the insertion of a TRUS transducer into the rectum, which is used to locate the prostate and house the biopsy needles. Tissue cores are obtained by inserting needles through the rectum into the prostate in a systematic

sampling scheme (figure 1.4). Ten to twelve cores are typically obtained with 1 to 2 cores per sextant of the prostate (left apex, right apex, left mid-gland, right mid-gland,

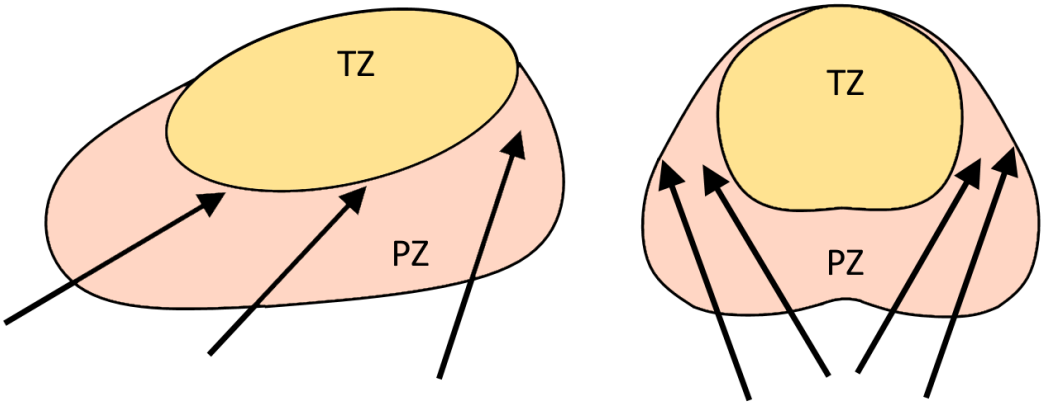

Figure 1.4 Typical random needle placement for a 12-core perineal TRUS-guided biopsy. Arrows show needle placement in the sagittal plane (left) and axial plane (right).

left base, right base) (19,20). Thus the procedure is image- guided in the sense that TRUS is used to locate the prostate, but the spatial distribution of tissue cores is predefined and the biopsy is not targeted.

This results in three common errors. Firstly, the biopsy may miss a clinically significant cancer due to under sampling. It has been reported that clinically significant tumors are missed in up to 30% of initial TRUS-guided prostate biopsies (21). Secondly, incorrect risk stratification can result from under-sampling a clinically significant lesion; if the lesion is sampled only at its periphery and thus comprises only a small portion of the core, it will be considered low volume. A study in 2010 reported that 46% of prostate cancer patients who were considered active surveillance candidates based on initial biopsy actually did not meet the Epstein criteria based on final histopathology (22).

Lastly, clinically insignificant disease can be detected by chance due to over-sampling. If this occurs, a larger number of cores containing cancer will be collected and the patient may not qualify for active surveillance, even though his cancer is indolent. A study reported greater than 17% of cases showed detection of insignificant cancer on initial biopsy (23).

Additionally, the range of biopsy needles is limited to the peripheral zone (PZ) in the posterior prostate. Since 80% of cancers occur in the PZ, this does not affect the detection of most cancers. It does, however, make the detection of cancers in the transition zone (TZ) especially difficult.

These limitations of a typical TRUS-guided biopsy have repercussions for patients and for the healthcare system. Patients undergoing a prostate biopsy risk experiencing side effects including persistant hematopermia (50.4%), hematuria (22.6%), fever (3.5%), urine retention (0.4%), and hospitalization due to complications (0.5-1.4%) (24). The biopsy and associated overdetection can be psychologically traumatic as well. This is particularly alarming when it has been reported that 75% of men who undergo biopsies have negative results (25,26).

Biopsies are also very expensive for the healthcare system. A budget impact analysis in 2012 calculated the total cost (sum of procedural cost and cost due to complications weighted by incidence) of a single biopsy to be $1946 (27). This contributes significantly to the greater than 15 billion dollar projected cost of prostate cancer care per year in the United States by the year 2020 (28).

1.3 Prostate Imaging

Imaging is a noninvasive means of acquiring information concerning the presence and extent of prostate cancer. Imaging modalities currently used for this purpose are TRUS, Computed Tomography (CT) and Magnetic Resonance Imaging (MRI). Of these, MRI has the benefit of not imparting doses of ionizing radiation to the patient while providing a higher sensitivity and specificity for prostate cancer diagnosis than the two other, cross-sectional imaging modalities.

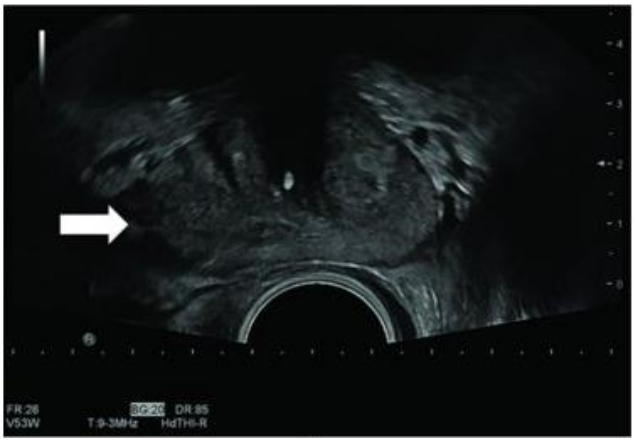

Figure 1.5 TRUS image of the prostate with a Gleason 7, biopsy confirmed tumor (29).

Before cross-sectional techniques were commonly used, intravenous urograms and micturing cystograms were used to image the prostate. In the 1960s TRUS became commonplace for biopsy guidance and then later to locate lesions (figure 1.5). The use of TRUS to image prostate cancer is limited, however, by low specificity due to the large number of isoechoic tumors in the PZ as well as the presence of hypoechoic benign nodules. TRUS is further unable to detect tumors in the TZ due to the heterogeneous appearance of BPH on ultrasound. Attenuation of the high frequency sonic waves used for TRUS further limits the ability to detect tumors in the anterior portion of the prostate.

Unlike TRUS, CT can be used to image a large field of view that encompasses the entire pelvis. Because of this, CT is used most prominently for radiotherapy treatment planning. CT is a 3D, tomographic imaging modality and therefore may provide better volumetric data and localization than TRUS and is easily able to image the entire prostate gland. Pixel intensity in a CT image is dependent upon the x-ray attenuation properties of the tissue and therefore provides a suitable map for planning geometries of radiation therapy beams or radioactive seed implants. CT may also be used to determine if cancer has spread outside of the prostatic capsule and/or to nearby lymph nodes. This is performed by identifying bulges along the border of the prostate and measuring lymph node diameter on the CT scan. The use of CT is limited, however, by its relatively high cost and its use of ionizing radiation. Beam hardening artifacts from the pelvis can make diagnosis difficult and CT suffers from too poor of diagnostic accuracy to be used for prostate cancer detection.

Figure 1.6 CT image of the prostate. Note the homogenous appearance of the prostate.

The diagnostic accuracy of MRI for prostate cancer surpasses that of CT due to its excellent soft tissue contrast and wealth of biologic information not available using many other imaging modalities. A conventional MRI exam, referred to as multiparametric MRI (mp-MRI), typically includes Dynamic Contrast Enhanced (DCE) MRI, Diffusion-Weighted (DW) MRI and T2-weighted imaging (T2WI). These techniques are described in more detail in 1.4. Magnetic Resonance Spectroscopic Imaging (MRSI) may be included to measure concentrations of metabolites within the prostate. These include citrate and polyamines, which are found in normal glandular tissue and heavily reduced in prostate cancer.

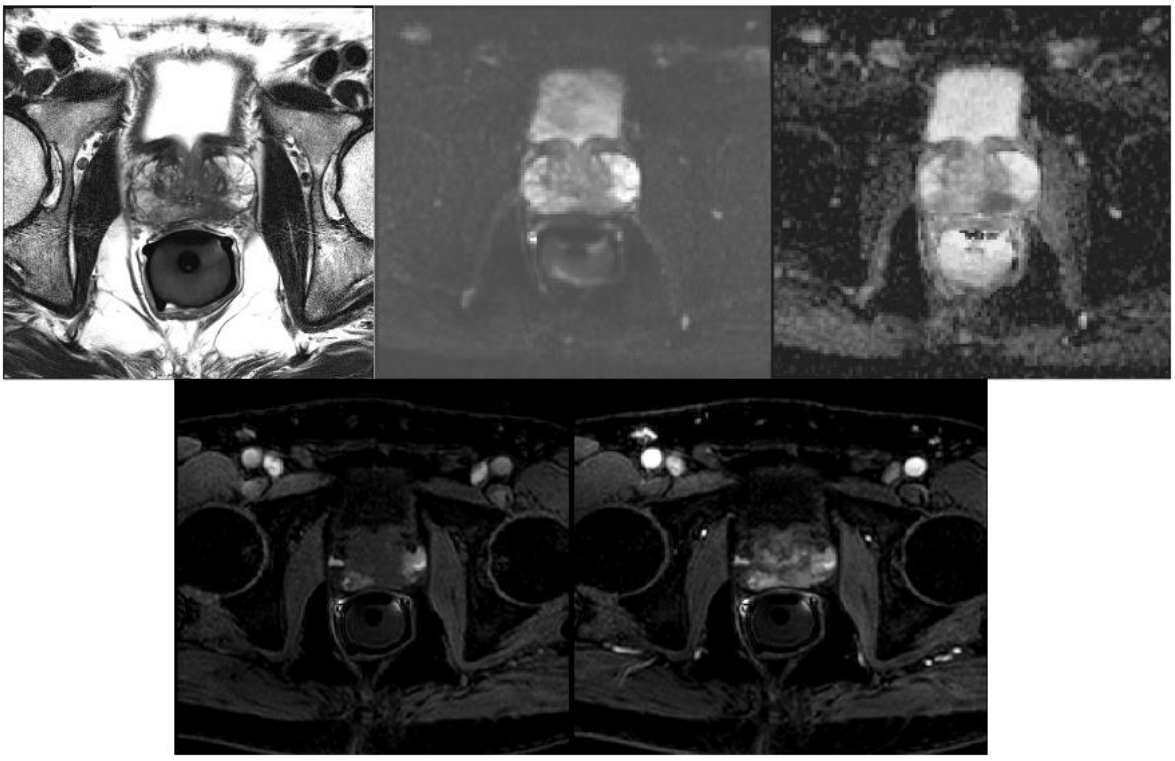

Figure 1.7 Multiparametric MRI of the prostate: T2-weighted image (top left), diffusion weighted image (top middle), ADC map calculated from DW-MRI (top right), T1 weighted image obtained pre-contrast injection for DCE- MRI (bottom left) and following contrast injection showing early enhancement of the prostate (bottom right). A cancerous region is apparent in the bottom [reader's] right of the prostate.

Using DW-MRI in conjunction with T2WI as part of a mp-MRI approach has been shown to significantly increase both sensitivity and specificity for cancer detection (30). Despite these improvements, the specificity and sensitivity achieved are not high enough for routine use, and limitations in these imaging techniques still restrict the clinical utility of mp-MRI. Better methods for distinguishing aggressive from indolent cancers are needed.

1.4 MRI

1.4.1 Basic MRI Theory

To produce MR images, magnetic fields and radiofrequency (RF) waves are applied to an object or patient and the magnetic response of the object or tissue is measured in the form of an induced current in surrounding coils. The signal generated depends on several factors including density of hydrogen nuclei and magnetic properties of the tissue.

The phenomenon behind MR Imaging is known as nuclear magnetic resonance (NMR). When placed in an external magnetic field (B_0), unpaired spins will align either parallel or antiparallel to the magnetic field and precess about the axis of the B_0 field. The parallel alignment represents a slightly lower energy state, so a small surplus of spins will assume this configuration. This surplus creates a net magnetization (M_z) parallel to the main magnetic field. The spins will precess about B_0 at a rate known as

the Larmor frequency, ω, dependent on the strength of the magnetic field and the gyromagnetic ratio, γ, of the nucleus.

$$\omega_0 = \gamma \cdot B_0.$$

If RF energy with frequency equal to the Larmor frequency is applied to the precessing spins, a time dependent magnetic field is produced about which the spins precess down into the transverse plane. The spins then decay back to the low energy states, parallel to the main magnetic field. The precession of spins in the transverse plane induces a current detected by coils placed around the object. As the spins return to the low energy configuration, their net magnetization in the transverse plane (M_{xy}) decreases and in the longitudinal orientation (M_z), increases. This behavior is described by the Bloch equations (below), and the rates at which these two phenomena occur are characterized by the T1 and T2 relaxation times.

$$\frac{dM_x}{dt} = \gamma \cdot M_y \cdot B_0 - \frac{M_x}{T_2}$$

$$\frac{dM_y}{dt} = -\gamma \cdot M_x \cdot B_0 - \frac{M_y}{T_2}$$

$$\frac{dM_z}{dt} = \frac{M_0 - M_z}{T_1}$$

If additional magnetic gradient fields with strength linearly related to position are superimposed, B_0, and thus the Larmor frequency, becomes a function of position. Applying a series of RF pulses with a range of frequencies then selectively excites subsets of spins with those Larmor frequencies. This allows for spatial encoding the signal detected in the coils surrounding the object.

This basic methodology can be applied to measure signal from any element in the body with net nuclear spin (Table 2). Conventional MRI measures hydrogen nuclei due to their natural abundance. Hydrogen nuclei consist of a single proton with a spin ½. Most importantly, water molecules contain two hydrogen nuclei. Additional contrast agents may be administered intravenously to perturb the magnetic field and influence the T1 and T2 relaxation times of the hydrogen nuclei.

Table 1.1 Nuclei in the human body which have a high enough abundance to detect with MRI.

Nuclei	**Unpaired Protons**	**Unpaired Neutrons**	**Spin**	**ϒ (MHz/T)**
^{1}H	1	0	1/2	42.58
^{19}F	1	0	1/2	40.08
^{31}P	1	0	1/2	17.25
^{23}Na	1	2	3/2	11.27
^{13}C	0	1	1/2	10.71
^{2}H	1	1	1	6.54
^{14}N	1	1	1	3.08

A diagram of MRI hardware components is shown in Figure 8. Multiple configurations of RF pulses, or pulse sequences, can be used to emphasize differences in proton density, T1 or T2 relaxation times between materials. This translates into different types and levels of contrast in resulting images allowing us to map even certain physiological properties in addition to anatomical information.

Figure 1.8 MRI Hardware: 1.5T Philips Achieva Scanner (Philips Healthcare, Best, Netherlands).

1.4.2 T1-Weighted Imaging

T1 relaxation, or spin-lattice relaxation, governs the return of the net magnetization vector to the longitudinal orientation. After the RF pulse tips the protons into the transverse plane, the protons release the absorbed RF energy into the surrounding lattice and return to the alignment parallel to the main magnetic field. This growth of the longitudinal component of the magnetization vector (M_z) following RF excitation to its maximum, equilibrium value (M_{eq}) is given by

$$M_z(t) = M_{eq} - \left(M_{eq} - M_z(0)\right) e^{-\frac{t}{T1}}$$

as derived from the Bloch equations. T1 is defined as the time it takes for the net longitudinal magnetization to reach 1-1/e (63%) of its equilibrium value following a 90°

RF pulse ($M_z(0)=0$). T1 contrast can be achieved using a Gradient Echo Pulse Sequence (figure 9) or a Spin Echo Pulse Sequence.

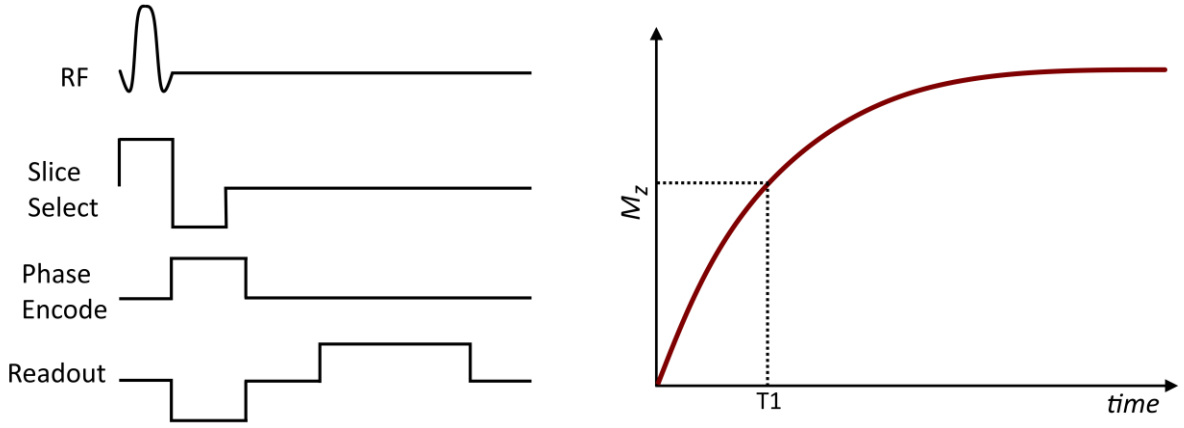

Figure 1.9 Gradient Echo pulse sequence diagram (left) and plot of T1 relaxation right); the net, longitudinal magnetization, M_Z, returns to its initial value following the RF pulse which tips the magnetization vector into the transverse plane. Tissue with a longer T1 will have a lower, net, longitudinal magnetization at time=T1 producing T1-weighted image contrast.

Two parameters of a pulse sequence which may be altered to influence signal and image contrast are echo time (TE) and repetition time (TR). TE is the time between the initial, RF excitation pulse and when the signal echo is received. TR is the time between consecutive RF excitation pulses. A T1 weighted image is acquired using a short TE to minimize the effects of T2 relaxation on the image contrast and a short TR relative to T1. Using a short TR ensures that magnetization is saturated and spins with a short T1 produce much more signal than spins with a long T1. By contrast, when TR is very long, detected signal is roughly proportional to equilibrium magnetization, which is similar for different tissue subtypes, and image contrast is poor.

It is also possible to create an image of measured T1 times within each voxel. This quantitative T1 map may be used clinically. To measure the T1 times within each voxel, a series of images are acquired with multiple TRs and the image data is fit to equation 4.

1.4.3 T2-Weighted Imaging

T2 relaxation, or spin-spin relaxation, is the loss of net magnetization in the transverse plane due to the dephasing of spins. When initially rotated into the transverse plane by an RF excitation pulse, all spins in the tissue have almost entirely the same phase. Immediately following the RF excitation, the spins begin to lose phase coherence as some precess slightly slower or slightly faster than others. This is caused by energy transfer between spins spurred by local magnetic field inhomogeneities from the precession of the spins themselves. The loss of phase coherence results in a decay of the net magnetization vector in the transverse plane (M_{xy}) given by

$$M_{xy}(t) = M_{xy}(0) \cdot e^{-\frac{t}{T2*}}$$

as derived from the Bloch equations. T2* is defined as the time it takes for the net transverse magnetization (MR signal) to reach 1/e (37%) of its initial value following a 90° RF pulse.

Phase coherence is also affected by small heterogeneities in the main magnetic field. Differences in susceptibility within the body introduce additional magnetism, which distorts the main magnetic field, causing the spins to dephase more quickly. The

combined effects of this dephasing due to magnetic field inhomogeneity (T2'), and pure T2 relaxation give the T2* time,

$$\frac{1}{T2^*} = \frac{1}{T2} + \frac{1}{T2'}$$

$$\frac{1}{T2'} = \gamma \cdot \Delta B_{inhom.}$$

where $\Delta B_{inhom.}$ is the inhomogeneity in the magnetic field in a voxel. T2* imaging is useful, particularly for perfusion imaging, susceptibility weighted imaging, and functional MR imaging (31). Its utility is limited, however, in the prostate where pure T2 imaging is preferable.

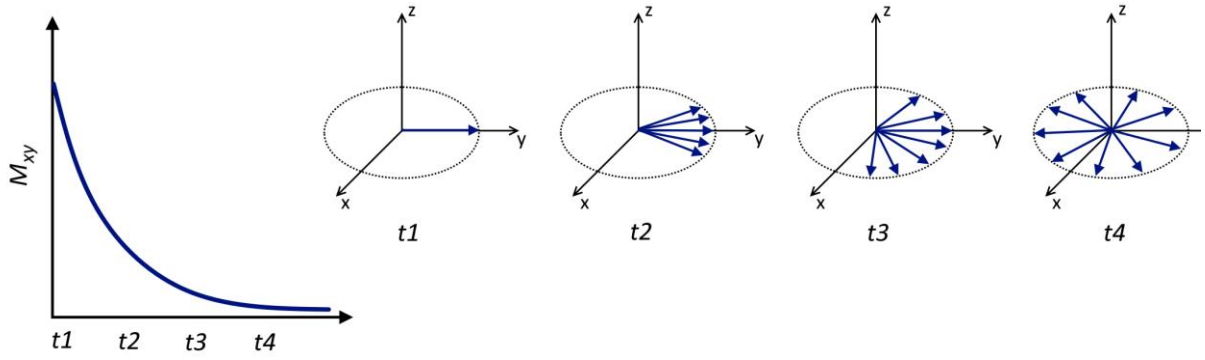

Figure 1.10 T2* relaxation; the net magnetization, M_{xy}, in the transverse plane decreases exponentially with time due to random dephasing of the spins.

Unlike pure T2 relaxation, T2' may be reversible (excepting loss of phase coherence due to diffusion as explained in 1.4.3). Whereas using a Gradient Echo sequence can only employ T2* contrast (by increasing TE), a Spin Echo sequence uses a refocusing pulse to obtain pure T2 contrast (figure 11). The refocusing pulse is

optimally a 180° RF pulse applied at half the TE. This pulse inverts the spins, which have dephased in the transverse plane so that they refocus at TE. This eliminates the T2* effects so that the subsequent dephasing is due solely to pure T2 decay.

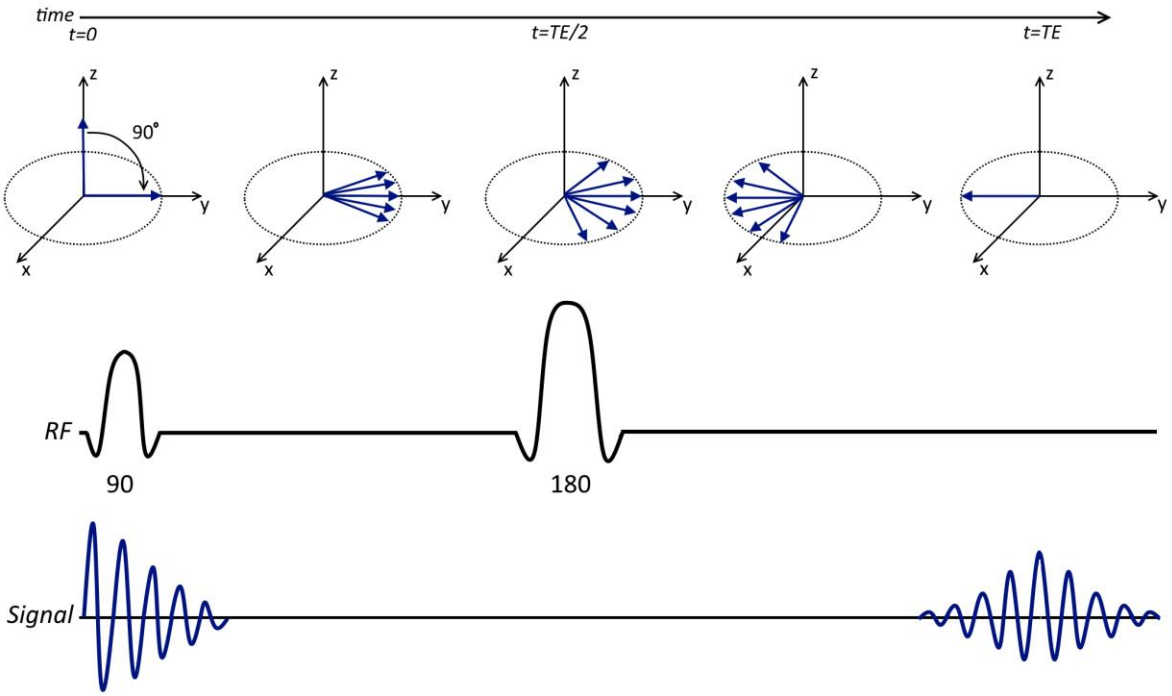

Figure 1.11 Effect of a refocusing pulse in a Spin Echo sequence. The magnetization vector, M, is initially parallel to the main magnetic field at time t=0. A 90° RF excitation pulse tips the magnetization vector into the transverse plane. The spins begin to dephase producing a free induction decay due to T2*. A 180° refocusing pulse applied at t=TE/2 inverts the spins and they refocus at time t=TE. producing an echo due to pure T2 relaxation.

A T2-weighted image is obtained by using a long TR to limit the influence of T1 relaxation on the image contrast and a long TE to allow the spins adequate time to dephase and produce strong T2 contrast. A T2 map may be generated by performing a series of Spin Echo sequences with varying TE and fitting the resulting image data to equation 5.

1.4.4 Diffusion Weighted Imaging

Diffusion Weighted Imaging uses the rate of water diffusion within different tissue environments to create image contrast. Water molecules in an unbounded compartment will undergo random, Brownian motion driven by fluctuations of thermal energy. This

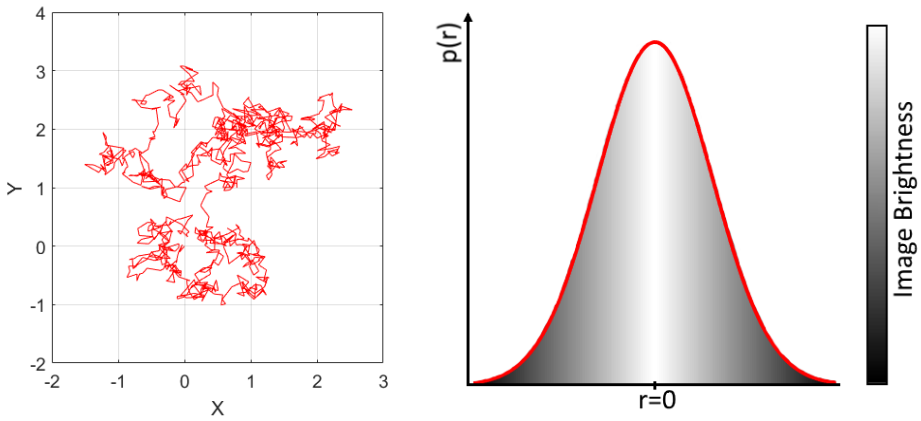

Figure 1.12 Example trajectory of a particle undergoing 2D Brownian motion for 1000 steps (left) and probability density function of its net displacement, r (right).

results in a Gaussian distributed net displacement (figure 12). If the range of the molecular diffusion is uninhibited by barriers, the extent of the Gaussian displacement will grow indefinitely. The presence of macromolecules will restrict the diffusion of the water molecules by slowing their motion through interactions and physical collisions.

In a magnetic field gradient, protons that diffuse along the gradient axis experience varying field strength. This affects the phases of the nuclear spins in the

transverse plane. When using a spin echo sequence, protons that are displaced due to diffusion will not be fully refocused by the 180° pulse; the total magnetic field they experience during the refocusing pulse will include position-dependent contributions from the gradient field. This lack of phase coherence decreases the observed signal, as observed by Hahn when he first proposed the Spin Echo sequence (32) and used it to measure diffusion rate.

Stekjal and Tanner took advantage of this effect to propose an acquisition method that gives signal magnitude dependent on diffusivity. After proposing the addition of a static “diffusion gradient,” they introduced a more effective, pulsed gradient method, which is the basis of diffusion sequences used today (33,34).

Current DWI sequences use Spin Echo sequences with strong, added diffusion gradients placed symmetrically about the 180° refocusing pulse (figure 13). The first diffusion gradient introduces a position-dependent phase offset in the protons. The second, identical diffusion gradient follows the 180° pulse and thus reverses the effect of the first diffusion gradient, provided the protons have not moved between the application of the gradient pulses. Protons with a net displacement along the gradient direction will experience a different field strength during the second gradient pulse. As a result, their frequency during the ‘rephasing’ portion of the spin echo will differ from their frequency during the ‘dephasing’ portion, and as a result magnetization will not be completely rephased by the refocusing pulse. This results in reduced spin echo signal intensity. By changing the strength (G), duration (δ) or time between the diffusion gradient pulses (Δ), different diffusion distances can be sampled. For simplification, these terms describing the diffusion gradients are contained in a single variable called

the b value. The measured signal as a function of b value then describes the diffusivity of water in the imaged environment, described by the Apparent Diffusion Coefficient (ADC):

$$\frac{S(b)}{S(0)} = \exp[-b \cdot ADC], \qquad b = -\gamma^2 G^2 \delta^2 \left(\Delta - \frac{\delta}{3}\right)$$

where S(b) is the measured signal at a particular b value. This monoexponential model assumes a homogenous medium with simple, unrestricted diffusion.

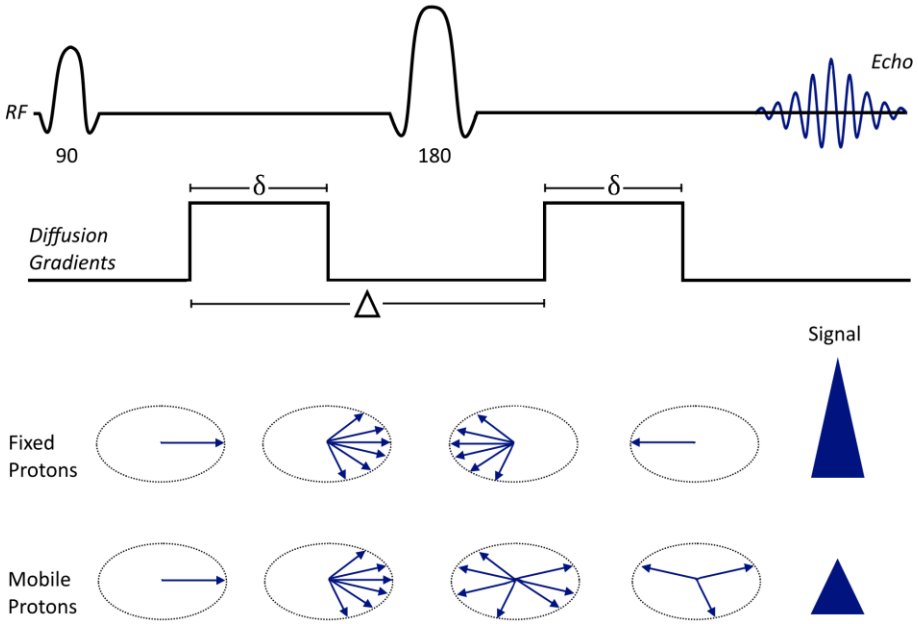

Figure 1.13 Diffusion Weighted Imaging sequence. Diffusion sensitive gradients are placed symmetrically about the refocusing pulse. Stationary protons which have dephased will be refocused by the 180° pulse. Mobile protons will not be fully refocused and have lower signal.

Diffusion imaging may be used to identify directionality of structural elements that inhibit diffusion anisotropically. This is particularly prominent in the brain where diffusion is directed along white matter tracts. For simplicity, diffusion is frequently treated as isotropic in body imaging. Gradients are applied along multiple axes and signal is averaged across acquisitions with different gradient orientations, giving equation 6.

Diffusion Weighted Imaging has become an important component of many body and brain imaging protocols. One drawback to this sequence is the requirement of large gradient amplitudes and rapid gradient switching. These induce eddy currents in metallic components of the scanner surrounding the magnet. The eddy currents in turn generate a magnetic field which adds to the gradient field creating distortions and image artifacts. Proper gradient shielding and adjustment of the gradient waveform to take into account expected eddy current contributions can diminish distortion to the waveform, but DWI remains more prone to these artifacts than other imaging sequences.

1.4.5 NMR Properties of Prostate Tissue

The differences in T1 and T2, which give rise to contrast in T1- and T2- weighted images, result from differences in molecular environment of the water molecules. Bound water is that which is found in the vicinity of macromolecules such as proteins and lipids. Its motion is constrained by interactions, namely hydrogen bonding, with the nearby macromolecules. This makes the transfer of energy in T1 and T2 relaxation processes efficient. Free water is composed of solely water molecules without the presence of macromolecules. The motion of the water molecules is not restricted, and they exhibit fast, disordered movement. As a result, the transfer of energy between

spins, which are fleetingly in contact, is inefficient and free water has a very long T1 and T2.

Following is a speculative description of histological properties of prostate tissues which likely give rise to appearance on MRI. These speculations are based on interpretations of current findings on prostate MRI and histology and not long-established facts. There is still much to learn on the nature of prostate tissue as well as NMR properties of water in intra- and extracellular environments.

The ducts of the prostate contain luminal fluid, which is primarily free water. This glandular tissue, found mainly in the PZ, has a long T2 and appears bright on T2 weighted images. The epithelium and stromal cell environment surrounding the ducts contain a larger portion of bound water in contact with the cell walls (extracellular and intracellular) and organelles (intracellular). Stromal tissue also dominates the TZ. While the luminal fluid dominates the signal in the PZ, the bound water in the stroma lowers the T2 of the TZ so that it appears darker on T2 weighted images.

Tumor growing into the lumen of the ducts reduces the luminal volume of prostate tissue. This reduces the signal contribution of luminal fluid, so that prostate cancer has a short T2 and appears dark on T2 weighted images. Rapid proliferation and dense packing of cancer cells also reduce the volume of extracellular fluid contributing to the shortened T2.

Similarly, luminal fluid has a high diffusivity and contributes heavily to the bright appearance of glandular prostate tissue on ADC maps. The dense cellular packing and

reduced luminal volume in tumor restrict the diffusion of water molecules. Thus, prostate cancer has a lower ADC and appears dark on ADC maps.

The primary use of T1 weighted imaging in prostate MRI is DCE-MRI. This imaging method is based on intravenous injection of a Gadolinium-based contrast agent. The Gadolinium ion contains 7 unpaired electrons making it paramagnetic; hydrogen nuclei in close proximity to the contrast agent will have shortened T1s and appear exceptionally bright on T1 weighted images. The rate at which signal enhances following contrast media injection reflects both blood flow and capillary permeability. Rapid proliferation of tumor cells necessitates increased blood flow and creates neovasculature, which is permeable and leaky. This causes the contrast agent to be taken up rapidly by the tumor relative to normal prostate tissue. Likewise, the contrast agent washes out quickly from the tumor through the porous capillary beds. Tumors can then be found by identifying areas of hyperintensity on T1 weighted images following an injection of contrast agent and analyzing the relative rates at which the signal intensity changes to estimate blood flow (perfusion) and capillary permeability.

1.5 Research Objectives and Scope of Dissertation

MRI is seeing increased interest from both patients and physicians for non-invasively monitoring and detecting prostate cancer (35-36). The expanded use of MRI could help reduce overtreatment rates and cut costs associated with unnecessary biopsies and prostatectomies. For MRI to become a widely used tool, however, better image acquisition and analysis methods are needed that give higher specificity and

sensitivity for diagnosis. A fundamental challenge of using MRI for prostate cancer detection is that small signals from multifocal cancers may not be detectable against the larger, background signal from normal tissue within a voxel. As discussed in 1.1, prostate tissue is comprised of a series of fluid-filled ducts surrounded by epithelial cells and stroma. Each of these tissue compartments contains individual populations of water molecules with unique sets of NMR features that all contribute to measured signal. By selectively filtering out particular compartments and detecting the change in signal, it is possible to emphasize a small signal component from prostate cancer that is otherwise obscured by background.

The aim of the research presented here is to investigate a hybrid, multidimensional imaging approach to prostate MRI, which looks at how standard measures (ADC, T1, T2) react to changes in sequence parameters (TE, TR, b). This enables a selective filtration of particular tissue components and subsequent emphasis of differences in tissue structure indicative of prostate cancer. These structural markers such as decreased luminal volume, increased cellularity, and nucleomegaly become more prominent with increased Gleason Score. Hybrid MRI may therefore be useful for noninvasively determining Gleason Score in the future.

Before quantitatively evaluating an imaging method or image-based parameter, it is necessary to establish the reproducibility of the method. The widespread use of diffusion-based imaging is a fairly recent occurrence. Although ADC is used clinically, its reproducibility has not been evaluated in prostate. In Chapter 2, I present such an assessment. Diffusion-weighted images are acquired back-to-back while the patient remains on the table in order to evaluate the short-term reproducibility of DW-MRI. This

represents the variability inherent to the imaging method due to physiological variation in the tissue. This type of variability cannot be mitigated by changing scanner parameters, and is a limiting factor in the use of ADC. This work was published in *Abdominal Imaging* (37).

Chapter 3 presents a pilot study on a novel, hybrid multidimensional T2-DW MR imaging method for prostate cancer. In this study I evaluate the role of a hybrid T2-diffusion weighted magnetic resonance (MR) imaging sequence for prostate cancer diagnosis and differentiation between aggressive and non-aggressive prostate cancer. This sequence gathers imaging data at a series of TEs and b values to measure the response of ADC and T2 to changing TE and b value, respectively. Populations of water molecules with distinct ADC-T2 pairings will respond differently to changing TE and b value. The hybrid T2-DW MRI sequence can therefore emphasize different compartments within prostate tissue and cancer which may otherwise be undetectable. This work is in press at the *American Journal of Roentgenology* (38).

Chapter 4 extends the hybrid imaging concept investigated in Chapter 3 to a combination of T1 and T2 imaging. A new hybrid T1-T2 imaging sequence collects images at a series of TEs and TRs. I detected changes in T1 with increasing TE and changes in T2 with increasing TR. Changes in T1 and T2 in response to these parameters suggest the presence of multiple compartments within the prostate tissue, some of which may be indicative of prostate cancer.

Chapter 5 discusses the significance of the research presented in this dissertation and potential further work in this direction.

CHAPTER 2

SHORT-TERM REPRODUCIBILITY OF APPARENT DIFFUSION COEFFICIENT ESTIMATED FROM DIFFUSION-WEIGHTED MRI OF THE PROSTATE

This chapter contains a reproducibility study of apparent diffusion coefficient in prostate using back-to-back DW- MRI scans. DW-MRI has become a staple of a standard, multiparametric MRI prostate exam. Despite its prominent clinical role, the reproducibility of ADC hasn't been fully characterized (53-8). As interest in both qualitative and quantitative assessment of diffusion-based imaging techniques increases, it is necessary to establish the reproducibility. Short-term variability in ADC is evaluated here in both cancer and normal prostate. Longer-term variability, such as inter-scanner and inter-patient deviations, will require a further study to quantify but such a study is beyond the scope of this dissertation.

2.1 Introduction

Diffusion weighted MR imaging has emerged as an important component of the multi-parametric prostate MR examination paradigm over the last decade (39-44). DW-MRI is a functional imaging method, providing information about changes in cellularity and vascularity which complements anatomical T2 imaging in prostate. Compared to other sequences such as DCE-MRI, DW-MRI requires no intravenous contrast injection, has the benefit of a short acquisition time, and does not require technically demanding

post-processing. The diagnostic efficacy of combining DW-MRI with T2 weighted imaging for prostate cancer detection has been proven in several studies. A meta-analysis performed by de Rooji et al. evaluated the diagnostic accuracy of combining functional imaging (DWI and DCE-MRI) with T2 anatomical imaging (35). Seven studies evaluating 526 patients imaged between 2007 and 2011 were included. Results showed a pooled sensitivity of 0.74 (95% Confidence Interval: 0.66-0.81) and a specificity of 0.88 (95% Confidence Interval: 0.82-0.92). For studies evaluating the PZ alone, sensitivity was 0.81 (95% Confidence Interval: 0.75-0.85) and specificity was 0.91 (95% Confidence Interval: 0.67-0.98).

Another meta-analysis performed by Tan et al. evaluated the performance of DW-MRI combined with T2 weighted imaging (30). This analysis included 19 studies with 5892 lesions. Results showed that the sensitivity and specificity of T2-weighted imaging improved from 0.57-0.62 and 0.74-0.78, respectively, to 0.69-0.72 and 0.80-0.85, respectively, when combined with DW-MR imaging. Even DW-MRI alone had a higher sensitivity and specificity (sensitivity: 0.67-0.72, specificity: 0.87-0.90) than T2 weighted imaging alone.

A study performed by Haider et al. evaluating the diagnostic accuracy of combined T2-weighted MRI and DW-MRI for localization of prostate cancer concluded that combined T2 and DW-MRI was better than T2-weighted imaging alone for prostate cancer detection within the PZ (39). This study evaluated 49 patients using whole mount histology of prostatectomy specimen as the reference standard and Receiver Operating Curve (ROC) analysis to compare mp-MRI with T2 weighted imaging alone. Area under the ROC Curve (AUC) was significantly higher for the combined T2-weighted and DW-

MRI than for T2-weighted images alone (AUC=0.89 vs. AUC=0.81, p=0.004). Sensitivity likewise increased with the addition of DW-MRI from 0.54 for T2 alone to 0.81 and specificity decreasing slightly (0.91 for T2 alone, 0.84 for combined T2, DW-MRI).

In addition to these studies evaluating DW-MRI combined with T2WI, quantitative analysis of diffusion-based image parameters has gained traction in recent years. Apparent diffusion coefficient (ADC) values obtained from DW-MR imaging have been shown to correlate with the Gleason scores of prostate cancer and D'Amico clinical risk scores (42, 44-7). A study performed by our group in 2011 compared parameters derived from DW-MRI and DCE-MRI with Gleason score and tumor angiogenesis based on whole mount prostatectomy specimen histology. Results showed that ADC correlated negatively with Gleason Score (r=-0.376, p=0.001). It was concluded that the moderate correlation between ADC and Gleason Score warrants further investigation on the potential of quantitative mp-MRI. A similar study published in 2015 by Hotker et al. found that ADC was significantly associated with all dichotomized Gleason Scores. In particular, tumor ADC gave an AUC of 0.693 for differentiating between Gleason 3+3 and Gleason 3+4 or higher cancers. ADC was the only parameter which showed a statistically significant difference between these two groups.

Recent studies have also shown that decreased baseline ADC values measured from prostate cancers of men who are active surveillance candidates are associated with tumor upgrade on repeat biopsy (48-9). These studies suggest that there may be a role for ADC to serve as a predictive biomarker in patients undergoing active surveillance.

Developing ADC as a quantitative imaging biomarker would allow better detection of prostate cancer by reducing inter-radiologist subjectivity. This subjectivity, i.e. differences in radiologists' interpretations of qualitative data, is a limit of qualitative evaluation of DW-MRI. A quantitative imaging biomarker is an image based parameter which is standardized and correlates with a pattern or condition. Developing ADC as a quantitative imaging biomarker could allow better differentiation of aggressive prostate cancer from indolent disease, thus reducing overtreatment while minimizing underdiagnosis (50).

A fundamental limitation of either qualitative or quantitative approaches to diagnostic characterization, however, is the lack of characterization of the reproducibility of the measurement. ADC values can be influenced by several imaging-dependent factors, such as gradient systems, coil systems, pulse sequence design, imaging parameters, and artifacts related to susceptibility effects or eddy currents (51). However, the variability of ADC values in normal prostate and prostate cancer has not been well established.

In this study we evaluate the short-term reproducibility of DW-MR imaging of the prostate in terms of changes in ADC maps between two consecutive scans without repositioning of the same patient using the same scanner and identical imaging parameters. Such an evaluation allows us to quantify the minimum expected variation in ADC maps, providing an effective lower bound on the uncertainty in DW-MRI acquisition. Clinically, this uncertainty represents the most fundamental limitation of DW-MRI usage; this is the component of variability that cannot be reduced by standardizing the imaging protocol or equipment. A second-phase study of long-term

reproducibility will be needed to account for variability from these sources as well as longer term biological variability, but is beyond the scope of this dissertation.

2.2 Materials and Methods

2.2.1 Study Subjects

Fourteen patients with biopsy-proven prostate cancer treated at our institution between April 2011 and September 2011 (age range: 38-80 years, median: 58.7 years; Prostate-Specific Antigen (PSA) level range: 4.5–12.7 ng/mL, median: 9.97 ng/mL; and Gleason score range: 6–8, median: 6.5) were evaluated under an Institutional Review Board-approved protocol. Informed consent was obtained from each patient and the study was compliant with the Health Insurance Portability and Accountability Act. All patients underwent a 12-core transrectal ultrasound (TRUS)-guided biopsy of the prostate (one medial and one lateral core in each sextant of the prostate: right base, left base, right middle, left middle, right apex, and left apex) and had at least one core that was positive for prostate cancer. Each patient underwent two identical DW-MR scans using spin-echo Echo-Planar Imaging (EPI) sequences (TR/TE 5000 ms/64 ms, b values of 0, 50, 150, 990 and 1500 sec/mm^2, 3 mm slice thickness, 26 slices, 1.5 mm x 1.5 mm in plane resolution, 128 x 128 matrix size, 180 x 180 mm^2 field of view, EPI factor 65, number of averages 4, scan time per sequence 7 minutes 25 seconds). The patient remained on the table between the scans to ensure that no significant prostate motion or deformation was introduced. All imaging was performed on a 3T Philips Achieva MRI scanner (Philips Healthcare, Best, Netherlands) using an endorectal coil in

combination with an 8-channel cardiac coil positioned around the pelvis. 1 mg glucagon (Glucagon; Lilly, Indianapolis, IN) was injected intramuscularly before scanning to limit peristalsis of the rectum.

2.2.2 Image Processing and Prostate Delineation

Following image acquisition, ADC maps were generated by using custom-built software written in MATLAB (Mathworks Inc., Natick, MA), that estimated ADC values via least squares fit of the negative log of the ratio of signal intensities, $-\ln(S_b/S_0)$, vs. b values.

A radiologist (Ibrahim Karademir, with 3 years of experience in prostate MRI) manually delineated the prostate on both series of DW-MR images for all patients by using a custom-written graphical user interface in MATLAB. Segmentation was performed on the b=0 sec/mm^2 image because these images had the highest signal intensity. A second radiologist (A.O. with 11 years of experience in prostate MRI) drew regions of interest (ROIs) of the cancerous lesions for 9 patients (Gleason Score 6-8, mean 7) based on the multi-parametric MRI results and 12 section TRUS guided biopsy results. Dark spots on the ADC map were outlined if there was a corresponding, hypointense, well-defined focus on T2 images and they were in a sextant with a positive biopsy core. The three-dimensional ROI volumes were delineated by using a Stentor PACS clinical software (Philips Healthcare, Best, Netherlands) on the b=0 sec/mm^2 images on the first DW-MRI sequence only.

2.2.3 Image Registration

To estimate the true difference in ADCs between the two consecutive scans, any variability due to motion must be removed. Factors such as bowel gas and patient discomfort may cause the prostate to shift between the first and second DW-MR scans, thus causing bias in a voxel-based analysis. We performed deformable registration between the two DW-MR image sequences using the open-source software package Plastimatch (v. 1.5.12-beta). For each patient, the prostate outlines on the ADC maps derived from the first and second DW-MR scans were overlaid on the corresponding, two, b=0 sec/mm^2 images. The surrounding tissue was masked out by setting image intensity to zero and the second image was registered to the first by using a Demons registration (52). The estimated deformation was then applied to warp the second-scan ADC maps onto the first-scan ADC maps. For each patient, an "ADC difference map" was then obtained by subtracting the two sets of ADC maps.

2.2.4 Data Analysis

The reproducibility of ADC values in the prostate was evaluated in terms of the ADC difference maps. The prostate volume was divided into sextants corresponding to the left base, right base, left medial, right medial, and left and right apex regions. The absolute ($|ADC_{scan1}-ADC_{scan2}|$) and relative percent differences ($\frac{|ADC_{scan1}-ADC_{scan2}|}{mean(ADC_{scan1},ADC_{scan2})}$) per voxel were then calculated across each of these regions as well as for the entire prostate. Additionally, the cancer ROIs were overlaid on the ADC difference maps and the per-voxel and per-ROI relative and absolute differences were calculated for the

cancer ROIs. Per-ROI differences refer to differences in mean values of ADC within an ROI.

2.2.5 Statistical Analysis

The differences between sextants were determined to be statistically significant or not using one way ANOVA. The significance level was chosen to be $\alpha<0.05$. The mean difference in each sextant per patient was calculated and listed as an independent measurement and ANOVA was performed on all six measurements.

2.3 Results

2.3.1 Overall Absolute and Relative Percentage Variations

The per-voxel absolute difference in ADC within the prostate ranged from 0 to 1.60×10^{-3} mm^2/sec (relative difference 0.00-200%, mean 10.52%). Table 1 shows the per-voxel ADC relative and absolute differences averaged across all patients within each sextant and over the entire prostate.

2.3.2 Variations within Sextant

The amount of variation in ADC did not change substantially with location in the prostate. The amount of variation was relatively uniform across the entire prostate with slightly higher variability seen in the apex. The largest difference was seen in the posterior apex (mean 11.55%). These results did not demonstrate a statistically significant difference in the level of variation between the different sextants. Variation in ADC within the apex, medial region, and base of the prostate is illustrated in figure 2.1

for a single patient.

Table 2.1 Voxel-to-voxel relative and absolute ADC variations within each sextant and the entire prostate across all patients

	Anterior Apex	Anterior Medial	Anterior Base	Whole Prostate
Relative Percentage Variation				
Mean Difference	10.6%	10.0%	10.8%	10.5%
Stan. Dev. of Difference	12.0%	12.9%	13.3%	12.0%
Median Difference	7.07%	6.42%	6.76%	7.05%
Absolute Variation (10^{-3} mm^2/sec)				
Mean Difference	0.103	0.100	0.116	0.117
Stan. Dev. of Difference	0.0980	0.104	0.154	0.125
Median Difference	0.0751	0.0699	0.0728	0.0802

	Posterior Apex	Posterior Medial	Posterior Base	Whole Prostate
Relative Percentage Variation				
Mean Difference	11.6%	10.5%	10.3%	10.5%
Stan. Dev. of Difference	12.5%	11.4%	10.6%	12.0%
Median Difference	8.00%	7.23%	7.24%	7.05%
Absolute Variation (10^{-3} mm^2/sec)				
Mean Difference	0.138	0.126	0.117	0.117
Stan. Dev. of Difference	0.135	0.129	0.113	0.125
Median Difference	0.0974	0.0878	0.0836	0.0802

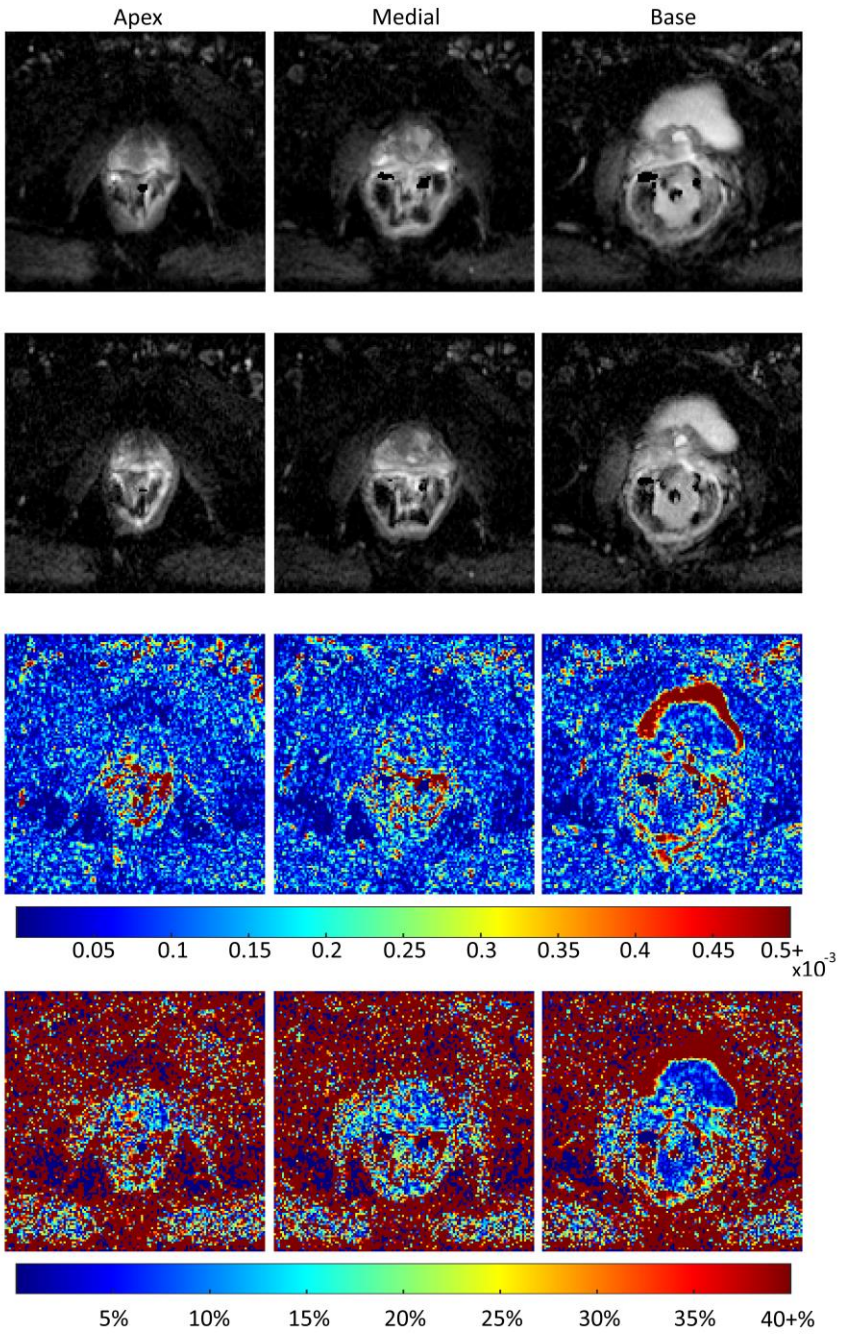

Figure 2.1 Axial ADC maps generated from back-to-back scans of a single patient (57 years, prostatic adenocarcinoma, Gleason score 8, PSA 10.37) through the center of the apex, medial section, and base of the prostate. Slices shown do not contain cancerous tissue. Absolute difference in ADC per voxel for corresponding slices are shown as well as relative percentage difference in ADC. High percentage variation shown outside of the prostate, particularly in the distal, left bladder may be attributable to motion effects and is not concerning as the ADC maps were registered using a warping template derived based on the masked prostate images, and do not take other tissues into account.

2.3.3 Variations within Cancer ROIs

Per-voxel analysis of the voxels located in cancer ROIs showed a mean and standard deviation in relative ADC difference of 17.15% ± 16.51%, respectively, higher than that of the whole prostate. The mean ± standard deviation of absolute voxel-by-voxel difference in cancer is $0.188 \pm 0.213 \times 10^{-3}$ mm^2/sec, and in the whole prostate is $0.117 \pm 0.125 \times 10^{-3}$ mm^2/sec (table 2).

Per-ROI analysis of the cancer ROIs showed the absolute ADC difference ranged from 0 to 0.463×10^{-3} mm^2/sec, with a mean of 0.122×10^{-3} mm^2/sec (1.02% to 37.7%, mean 10.6%). Figure 2.2 shows an example of variation within a cancer ROI and surrounding prostate tissue for a single patient.

Table 2.2 Relative percentage and absolute difference in ADC for cancer ROIs and whole prostate derived using voxel-based approach, and relative percentage and absolute difference in mean ADC of cancer ROIs between the two scans. All medians are taken of the non-negative, magnitude differences.

	Absolute (mm^2/sec)		Relative Percentage	
	Range	Median	Range	Median
Per-voxel Variation				
Cancer ROI	$[1.07 \times 10^{-6}$, $8.41 \times 10^{-4}]$	9.67×10^{-6}	[0.00% , 67.37%]	11.2%
Whole prostate	$[2.33 \times 10^{-10}$, $1.60 \times 10^{-3}]$	8.02×10^{-5}	[0.00% , 200%]	7.05%
Per-ROI Variation				
Cancer ROI	$[-4.22 \times 10^{-4}$, $4.63 \times 10^{-4}]$	3.63×10^{-5}	[-32% , 37%]	4.18%
Mean + S.D. ADC:	$3.78 \pm 4.79 \times 10^{-4}$ mm^2/sec			

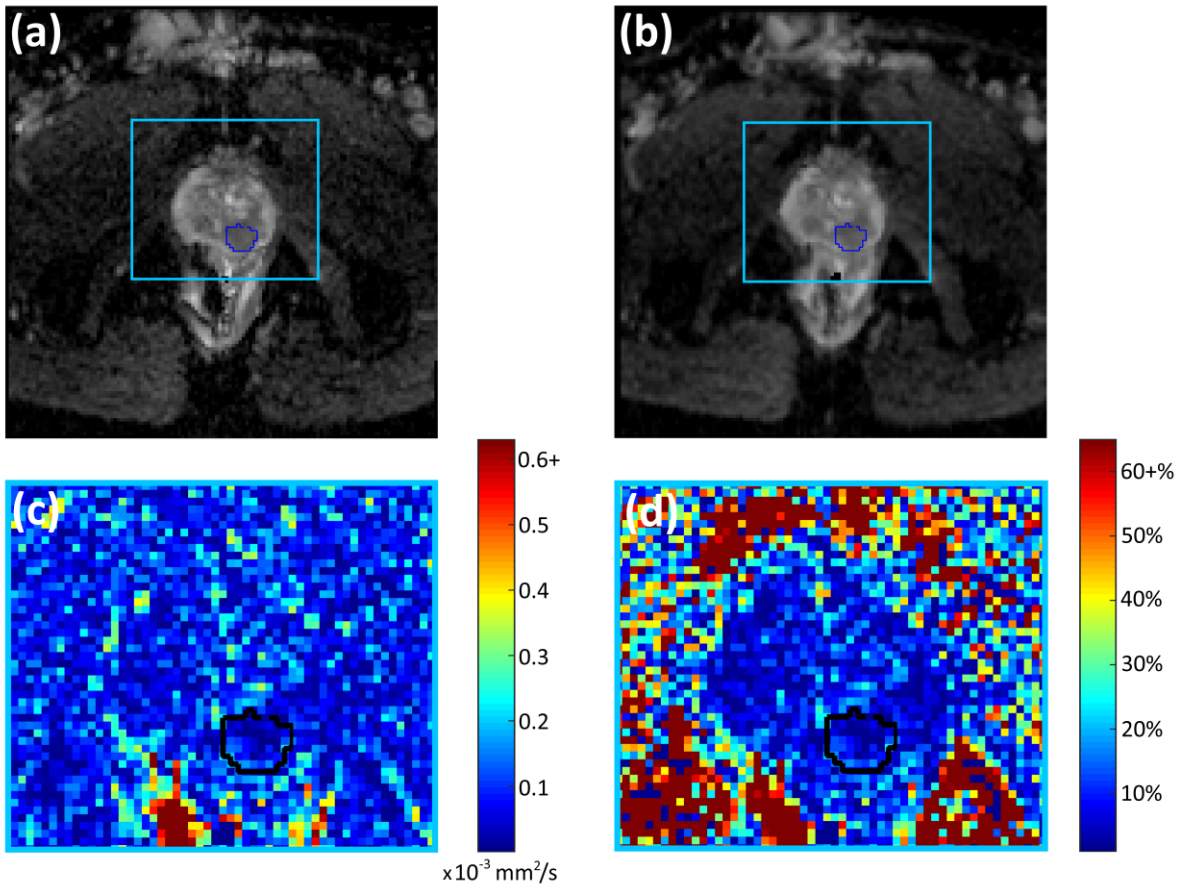

Figure 2.2 (a-b) pair of axial ADC maps generated from back-to-back DW-MR images for a single patient (55 years, prostatic adenocarcinoma, PSA 12.7) with cancerous ROI outlined in blue, (c) absolute difference in ADC between scan a and scan b for area within light blue box, and (d) relative percentage difference in ADC between scan a and scan b for area within light blue box. High areas of variability are common outside of the prostate, particularly in the rectum, and relative variation is high outside of the prostate where the signal intensity is very low. Although the variability in ADC is low within the prostate there are foci of 25 to 30% visible, demonstrating how variability within DW-MRI may affect not only quantitative imaging results, but also results of a qualitative, clinical assessment.

2.4 Discussion

Our results suggest that the reproducibility of ADC measurements in prostate is reasonable. The posterior prostate consistently showed higher variability than the anterior portion which may be attributable to the influence of the rectum. However, we were not able to demonstrate statistical significance in the variations between sextants.

Chenevert and Malyarenko have both performed studies evaluating the repeatability of ADC measurements made using ice water phantoms and found variability to be less than 5% (53-4). Chenevert evaluated 20 MRI scanners from 3 vendors over 25 days with a phantom of distilled water in an ice water bath and found that reproducibility in ADC for a single system was within ±5%. Malyarenko performed a study in which a DW-MRI exam was performed on an ice water phantom at 35 institutions on 3 different vendor systems, each exam consisting of 4 back-to-back DW-MRI acquisitions. Intra-exam repeatability of ADC values, defined as 2 standard deviations in ADC expressed as a percentage of mean ADC, was found to be within 1% (i.e. 95% of measurements are expected to fall within 1% of the mean) for 70 ROIs drawn within the phantom. Comparing with the results of these phantom studies, we consider the reproducibility demonstrated in our study to be reasonable.

Our results show lower variability in ADC than recent reports of reproducibility in the abdomen and liver (55-56), which show variability of 25-30%. Our study is unique in evaluating back-to-back prostate scans while the patient remains on the table, thus eliminating effects of scanner variability over time and inter-scanner and patient variability from repositioning the patient in the scanner. These sources of variation that

were not considered in this study have been evaluated recently in other studies. Litjens et al. performed a study on 51 patients with prostate cancer in the peripheral zone and another 10 patients with high PSA levels but negative TRUS-guided biopsy results to determine inter-patient variability of ADC in the peripheral zone and its effect on the prediction of prostate cancer aggressiveness, by comparing median ADCs within an ROI between repeat imaging scans (57). Results of this study indicate that ADC measurement variability in normal peripheral zone tissue attributable to coil and imaging sequence parameter choices was significantly lower (p=.0058) (mean 0.068 x 10^{-3} mm^2/sec ± 27 x 10^{-3}) than inter-patient variability that they hypothesized attributable to tissue physiological variations (1.2-2.0 x 10^{-3} mm^2/sec). Gibbs et al. evaluated the reproducibility of DW-MRI of the prostate in a study of 8 healthy volunteers undergoing two DW-MRI sessions timed approximately one month apart, with each volunteer scanned twice in the second session. ROIs were outlined in the prostate for comparison of ADCs. Results indicate that both short and medium-term repeatability (defined as 2.77 times the within-subject standard deviation) were under 35% (58).

Motion and deformation of the prostate inevitably have influence on a reproducibility study. We minimized such effects by performing deformable registration, however, it is impossible to completely remove motion-related variability. Glucagon was also injected immediately before the MR exam to limit peristalsis of the rectum but due to the nature of the study in which the patient remained on the table between scans and time between scans was minimized, it was not practical to re-administer glucagon between scans. Thus, it is possible that the true short term variability may be slightly

lower than that reported here. Note also that the time between our back-to-back image acquisitions was so small that motion between the consecutive scans was minimal.

Limitations of our study include a limited number of study patients. Also, our reference standard was TRUS guided biopsy results rather than histopathology. This may be important for our analysis of the cancer ROIs, but is likely not critical for our analysis of the reproducibility over the entire prostate. Lastly, in this study we evaluated only short-term reproducibility and did not evaluate contributions from scanner model, coil choice, and imaging parameters, etc. Future studies that take into account of the contributions from all of these sources will be necessary, particularly for using ADC as an imaging biomarker because reproducibility between institutions and scanners will be important.

2.5 Conclusion

ADC has strong potential to become a powerful quantitative imaging biomarker for prostate cancer but it is important to understand the reproducibility of DW-MR imaging for this potential to be realized. Our results show that minimum ADC variation within the prostate is reasonable, on the order of 10%, and lower than those reported for other abdominal organs. This study of an evaluation of short term reproducibility is a first step towards a more comprehensive assessment of the reproducibility of DW-MR imaging of prostate cancer.

CHAPTER 3

PILOT STUDY OF THE USE OF HYBRID MULTIDIMENSIONAL T2-DW-MRI FOR DIAGNOSIS OF PROSTATE CANCER AND EVALUATION OF GLEASON SCORE

In this chapter, I present a study demonstrating the use of a hybrid T2-Diffusion Weighted MRI sequence for evaluating the aggressiveness of prostate cancer. As discussed in Chapter 2, mp-MRI including DW-MRI has become a staple of prostate cancer imaging. The use of prostate MRI is, however, still limited. One of the limitations is that the small signal from a dispersive prostate cancer may be eclipsed by a larger background signal within an imaged voxel. I present the analysis of a novel sequence which uses the interdependence of ADC and T2 to selectively filter background signal and potentially isolate signal within a voxel corresponding to a tumor environment. Hybrid T2-DW MRI measures the response of ADC and T2 to changing TE and b value, respectively. This approach shows promise for detecting prostate cancer and determining aggressiveness non-invasively.

3.1 Introduction

As discussed in Chapter 2, multi-parametric MRI (a combination of T2-weighted, diffusion weighted (DW-MR) and dynamic contrast enhanced MRI (DCE-MRI)) is commonly used for diagnosis, local staging and detection of prostate cancer (59-66). T2-weighted and DW-MR images are the backbone of this protocol (67-68) and their

combination improves diagnostic accuracy over T2 weighted imaging alone. While these results are encouraging, higher sensitivity and specificity are needed for routine clinical applications of MRI.

In studies evaluating the efficacy of combining T2 weighted and DW-MR imaging, T2 and ADC have been measured independently and assumed independent within a voxel. Current clinical standards call for a T2 weighted imaging sequence to be performed by acquiring data at a series of TE values without the application of a diffusion gradient. Similarly, DW-MRI involves the acquisition of data at a series of b values with a constant, minimal TE throughout acquisition. By increasing the b value or the TE value, one is able to isolate the components within a voxel with restricted diffusion or long T2, respectively. In this conventional, multiparametric approach, one is able to isolate these components individually, but their interdependence is neglected. T2 is calculated without taking into account the dependence of T2 on b value. Similarly, ADC is calculated without accounting for the dependence of ADC on TE. ADC and T2 are therefore implicitly assumed to be independent (67-69). Previous studies demonstrated that T2 and ADC are frequently interdependent, and distinct populations of water molecules in each voxel with specific paired T2 and ADC values can be identified (70-74).

Neurological studies modeling ex vivo tissue samples of bovine optic nerves and in vivo acute cerebral infraction, and work presented by Does and Gore for studying ischemia in rat brains, have suggested that ADC and T2 values are often coupled in these environments; different populations of water protons within a voxel display specific combinations of ADC and T2 which may be used to identify these individual

distributions within a voxel which are often heterogeneously distributed on a microscopic level within a voxel. Does and Gore demonstrated that relative signal contributions of different compartments within rat brain tissue can be manipulated by changing TE and b value using what they termed “hybrid diffusion weighted imaging,” so that ADC and T2 are dependent on TE and b value. This suggests that measuring signal at multiple TE and b values for each voxel, yielding an array of imaging data at combinations of TE and b value, allows for isolation of different compartments based on differing signal contributions and thus evaluation of the microscopic heterogeneity of water proton populations on a sub-voxelar level.

A pilot study demonstrated that hybrid imaging may improve the accuracy of MRI in diagnosing biopsy-proven Prostate cancer, by exploiting the interdependence of ADC and T2 (75). Hybrid imaging identifies sub-voxelar populations of water molecules within the prostate based on changes in the measured T2 and ADC in response to changes in ‘b’ and TE respectively. This approach has the potential to isolate a relatively small signal from cancerous foci within a voxel from a large background signal corresponding to normal glandular tissue.

In the current study, we build upon previous work with an expanded patient data set and Gleason score information obtained from prostatectomy to evaluate cancer aggressiveness. Our purpose was to investigate the potential role of a novel, hybrid T2-diffusion-weighted MR imaging sequence in diagnosis of prostate cancer and differentiation between aggressive and non-aggressive prostate cancer.

3.2 Materials and Methods

3.2.1 Patients

Twenty one consecutive patients referred to the Department of Radiology at our institution between June 2012 and May 2013 for a diagnostic MRI of the prostate were recruited for and consented to this study. The study was approved by our Institutional Review Board and was Health Insurance Portability and Accountability Act-compliant. Inclusion criteria for the patient were: (a) patient received a positive transrectal ultrasound (TRUS)-guided biopsy positive for prostate cancer, (b) patient received a radical prostatectomy following the imaging exam with the prostatectomy specimen positive for prostate cancer, (c) patient was scanned with hybrid T2-diffusion weighted MR imaging at our institution following biopsy and preceding prostatectomy. From the 21 patients recruited, 40 cancerous regions were identified (Gleason score range: 6-9, median: 7). MR imaging was performed on a Philips AchievaTX 3 Tesla scanner (Philips Healthcare, Best, Netherlands).

3.2.2 MR Image Data Acquisition

Each patient received a multiparametric MRI exam which consisted of: T2 weighted turbo spin-echo (TSE) sequences, T1 weighted TSE sequence, T2 mapping, DCE-MRI sequence and hybrid T2-diffusion-weighted hybrid sequence. All images were acquired with free-breathing. The hybrid sequence consisted of a series of standard pelvic prostate DW-MRI protocol pulse sequences composed of a spin echo module with diffusion sensitizing gradients placed symmetrically about the 180 degree pulse followed by single shot echo-planar imaging (EPI) for signal detection. This pulse

sequence was used to acquire images with TEs of 47, 75 and 100 ms, and images at each TE were acquired with b values of 0 and 750 s/mm^2, resulting in a 3x2 array of data associated with each image voxel. Hybrid images were acquired in the axial plane oriented perpendicular to the rectal wall, as guided by sagittal images. Fat saturation was implemented by using spectrally adiabatic inversion recovery (SPAIR). Scan time was 7-9 minutes per sequence and in-plane resolution was 2.5 mm x 2.5 mm. Hybrid sequence parameters are listed in Table 1. An endorectal coil (Medrad, Bayer Healthcare, Warrendale, PA) and a 6-channel, cardiac, phased-array coil placed around the pelvis were used to detect signal. A dose of 1 mg glucagon (Glucagon, Lilly, Indianapolis, IN) was injected intramuscularly immediately before the MRI scan to limit peristalsis of the rectum.

Table 3.1 Hybrid T2-diffusion weighted MRI sequence parameters

Hybrid T2-DW MRI Protocol	
TE	47, 75, 100 ms
b values	0, 750 sec/mm^2
TR	3000 ms
Number of Slices	20-25
Slice thickness	3 mm
In-plane resolution	2.5 mm x 2.5 mm
Matrix size	128 x 128
Field of view	180 x 180 mm^2
NEX	4
SENSE Factor	2
Received Bandwidth	3307.5 Hz
Scan time per sequence	7 – 9 min

3.2.3 Histology-MRI Correlation

Following the MRI exam, histologically confirmed tumors were mapped onto the hybrid T2-DW images. Prostate cancer foci and regions of normal prostatic tissue were

identified and defined through a correlative review of each prostatectomy specimen and the corresponding MR images by a genitourinary pathologist (Tatjana Antic, 9 years of experience in genitourinary pathology) and a radiologist (Aytekin Oto, 10 years of experience in prostate MR imaging). Each prostatectomy specimen was sectioned serially into 4 mm thick slices from apex to base in transverse planes. Slices were halved or quartered and fixed in 10% buffered formalin. The blocks were embedded in paraffin and 4-5 µm microtome slices were extracted and stained with hematoxylin-eosin.

The pathologist first identified all distinct tumor foci with diameter larger than approximately 5 mm in all specimen block sections for each patient. The pathologist assigned Gleason score to each cancer focus. Then, the radiologist and pathologist, in consensus, identified the MRI slice (T2-weighted image or ADC map) that matched the level of the pathology slice where the cancer focus was detected. Once, this was achieved the radiologist then manually delineated regions-of-interest (ROIs) of cancer foci on MR images which corresponded with the location of the cancer on histopathology. If the tumor focus was not apparent on MR images, its location was determined from spatial relationship to identifiable anatomic landmarks such as the urethra, a BPH nodule with distinct characteristics or ejaculatory ducts. All tumors in both the peripheral zone and central gland that were identified on histology specimens were delineated on the MR images. Regions of prostate defined as normal tissue were also outlined unless no normal locations could be found in the prostate. A location was defined as normal by the pathologist if cancer or high-grade prostatic intraepithelial neoplasia, benign prostatic hyperplasia, prostatitis or other benign abnormalities were

not present. ROIs were delineated on either an ADC map or T2-weighted image based on which image set showed better correlation with the histologic findings.

3.2.4 Transfer of ROIs

The ROIs were transferred to the hybrid image set semi-automatically using custom software written in Matlab (Mathworks, Natick, MA). The software transferred the ROIs from the images on which they were delineated to the coordinate system of the hybrid scans based on the scanning geometry information. This procedure was based on the assumption that there was no patient motion between MR sequences. Following registration, the transferred ROIs were reviewed on the hybrid images by a radiologist (A.O.) for accuracy. If there was visually obvious misalignment, the ROI position was manually adjusted in three dimensions without changing the shape or size of the contour.

3.2.5 Quantitative Image Analysis

T2s and ADCs were estimated from the hybrid image set using least squares regression. ADC was calculated at each TE using both b values according to the formula:

$$S(t) = A\exp(-b \cdot ADC(TE))$$

T2 was calculated at each b value using all TE values according to the formula:

$$S(t) = A\exp\left(\frac{-TE}{T2(b)}\right)$$

Both ROI and voxel based fits were performed. ROI based fits were performed by averaging the signal intensities across all voxels within an ROI and performing a single fit to these averaged values. These fits yield a 3 x 2 imaging data grid with ADC at TE=47, 75, and 100 ms and T2 at b=0 and 750 s/mm2. If signal intensity within a voxel increased with increasing b value or TE, data from that voxel were considered corrupted and excluded from the analysis. One or more voxels were excluded in 17 out of 59 ROIs.

The dependence of ADC and T2 on TE and b value, respectively, was evaluated by comparing ADC at different TEs and T2 at different b-values for normal and cancerous ROIs. Linear discriminant analysis (LDA) was employed to create a classifier to differentiate between Prostate cancer and normal tissue. The LDA was constructed from the three ADCs and the two T2s associated with each voxel. As a result, the LDA included not only the baseline ADC and T2 but also the change in T2 and ADC when b-value and TE are increased. ROI-based ADC and T2 fits were used and ADCs and T2s were normalized using min-max scaling to range from 0 to 1. The effectiveness of the classifier was evaluated by using the 'leave one out' cross validation and ROC analysis and compared to baseline ADC (TE=47 ms) alone.

An additional parameter, referred to in the following as 'PQ4', was calculated to reflect the response of ADC to changing TE and the response of T2 to changing b-value. This was defined as the percentage of voxels within a single ROI which display an increase in T2 when b value is increased from 0 to 750 s/mm^2 and a decrease in ADC when TE is increased from 47 to 75 ms. This is the opposite of the observed change in T2 and ADC with changing b value and TE in normal prostate. These voxels

appear in Quadrant 4 of plots of ADC(TE=75 ms) – ADC(TE=47 ms) vs. T2(b=0 s/mm^2) – T2(b=750 s/mm^2) (figure 3.1), and thus the percentage of voxels with these characteristics is referred to as 'PQ4'. The voxel-based ADCs and T2s were used for calculation of PQ4. The value was compared for cancers vs. normal tissues as well as cancers of different Gleason scores. PQ4 was also compared to ROI-based ADC and T2 values at each TE and b value for all ROIs.

3.2.6 Statistical Analysis

The Mann Whitney U test was used to compare ADC or T2 values between cancer and normal ROIs at each TE and b value, respectively. This nonparametric test evaluates the null hypothesis of two samples coming from the same population against the hypothesis that there are two populations with one tending to have larger values. This test was unpaired. Student's t test for paired data was used to compare T2 values measured at each b value between cancer and normal ROIs. This test was chosen since our data is unpaired and normally distributed with only two sample populations. The Friedman test, a non-parametric rank based test, was used to compare ADCs at different TE values between normal and cancer ROIs. This test is appropriate for comparing more than two sample populations and repeated measures. The area under the curve (AUC) was calculated for both the LDA classifier and the baseline ADC alone by using the proper binormal model (17). Student's t test was used to compare PQ4 between cancer and normal ROIs and Spearman's rank order correlation coefficient was calculated between PQ4 and Gleason score. Spearman's rank-order correlation is a non-parametric test which evaluates the strength of association between, in our case, a nominal and an ordinal variable. All p-values were two sided and were calculated from

ROI-based fits for ADC and T2, with the exception of PQ4, which was from voxel-based calculations. A Bonferroni correction was applied for 16 multiple comparisons and effectively set the alpha level for statistical significance at $\alpha=0.0031$.

3.3 Results

The dependence of T2 on b-value and ADC on TE is shown in Table 2 for all cancer and normal ROIs. ADC was significantly higher in normal ROIs than in cancer ROIs at all TEs ($p < 0.0001$). T2 was significantly longer in normal ROIs than in cancer ROIs at both b values ($p \leq 0.0002$). The mean ADC in cancer ROIs increases by only 3% when TE is increased from 47 ms to 75 ms. In contrast, the mean ADC in normal ROIs increases by 12% (figure 3.2). This results in a difference in mean ADC of cancer and normal ROIs at TE=75 ms of 0.70×10^{-3} mm^2/s, or approximately 60%. This difference is highly significant with $p<0.0001$. Mean T2 in both normal and cancer ROIs decreases with increasing b value. The decrease in mean T2 is larger in normal ROIs ($\Delta T2=-52$ ms) than in cancer ROIs ($\Delta T2=-17$ ms).

Table 3.2 Mean and standard deviation of ADC and T2 as a function of TE and b-value across all patients.

	Normal (n=19)	**Cancer (n=40)**	p value*
ADC (10^{-3} mm^2/s)			
TE=47 ms	1.61 ± 0.32	1.08 ± 0.28	*<0.0001*
TE=75 ms	1.81 ± 0.34	1.11 ± 0.26	*<0.0001*
TE=100 ms	1.85 ± 0.36	1.23 ± 0.33	*<0.0001*
p value†	*<0.0001*	*<0.0001*	
T2 (ms)			
b=0 mm^2/s	146 ± 74	81 ± 54	*<0.0001*
b=750 mm^2/s	94 ± 41	64 ± 19	*0.0002*
p value†	*<0.0001*	*<0.0001*	

Note.—ADC and T2 values are from ROI-based fits.

* *P values compare cancer vs. normal ROIs (column) derived from Mann Whitney U test.*

† *P values compare ADCs at different TEs and T2s at different b values (rows), derived from the Friedman rank sum test and paired t test, respectively.*

The AUC for differentiating cancer from normal tissue of the LDA classifier was 0.96 compared to 0.91 for the baseline ADC alone (figure 3.4). PQ4, the percentage of voxels in each ROI for which T2 increased with increasing b-value and ADC decreased with increasing TE differentiated cancer from normal tissue (figure 3.1). The mean PQ4 was 3 ± 6% for normal ROIs (n=19), and 19 ± 24% for cancer ROIs (n=40). This difference was statistically significant with $p=0.0004$.

PQ4 also showed a significant correlation with Gleason score (figure 3.5). The mean value of PQ4 was 9.5% for Gleason 6 cancers, 22.6% for Gleason 7 cancers, and 30.0% for Gleason 8-9 cancers. This trend is statistically significant with a Spearman coefficient of $\rho=0.508$ indicating a significant linear trend, with $p<0.0001$.

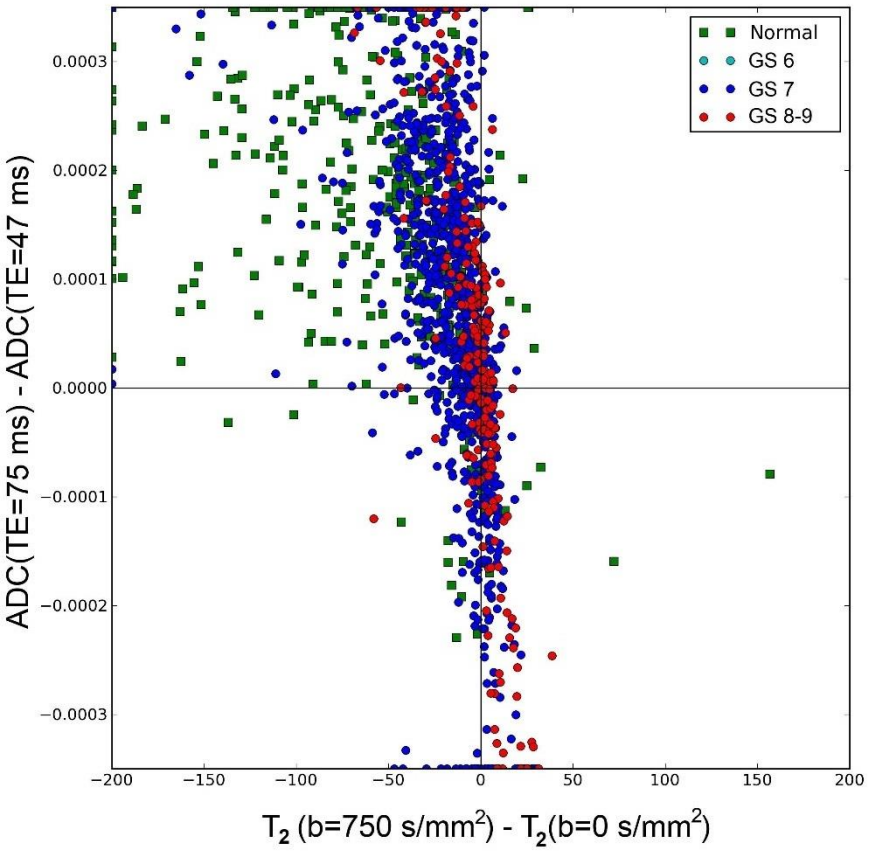

Figure 3.1 Response of ADC and T2 in voxels across all patients and ROIs to increasing TE and b-value. Each marker represents a single voxel. Almost all of the normal voxels are in Quadrant 2 (upper left). Quadrant 4 (lower right) contains an increased number of voxels as Gleason score increases.

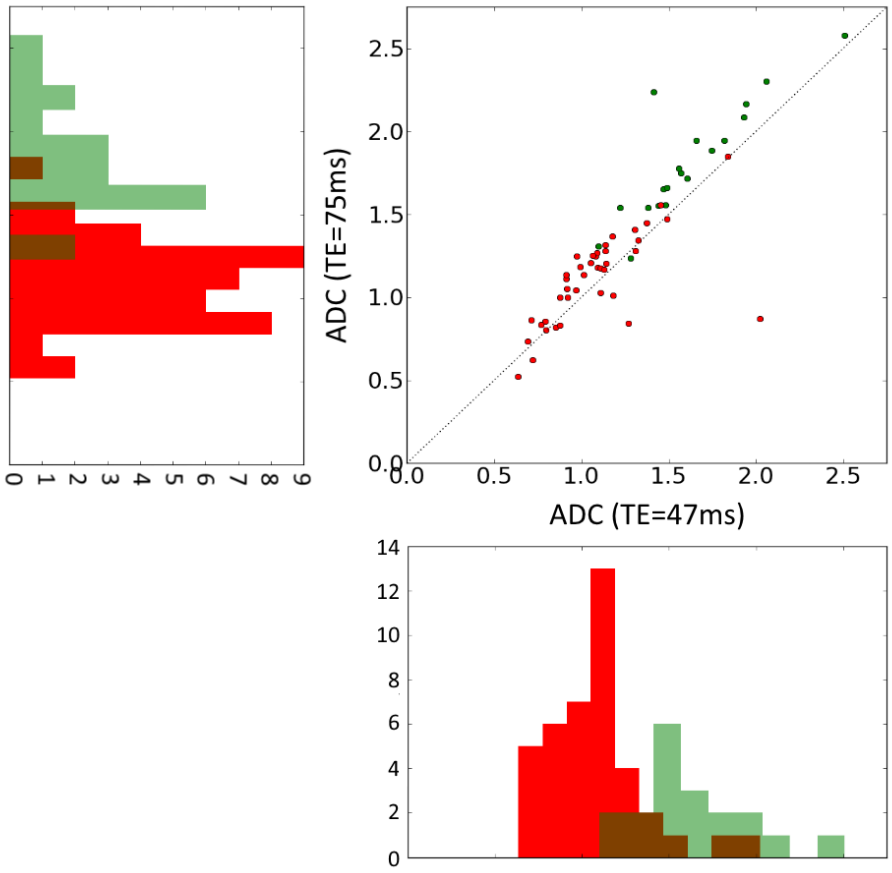

Figure 3.2 ADC (10^{-3} mm^2/s) of cancer (red) and normal (green) ROIs at TE=75 ms vs. ADC at TE=47 ms. Each point refers to one ROI. Histograms on the x and y axes show collapsed data along respective axes. Overlapping regions of the histograms are shown in brown. The difference in the distributions of ADC demonstrate the improved performance of ADC at TE=75ms over ADC at TE=47ms in our data set.

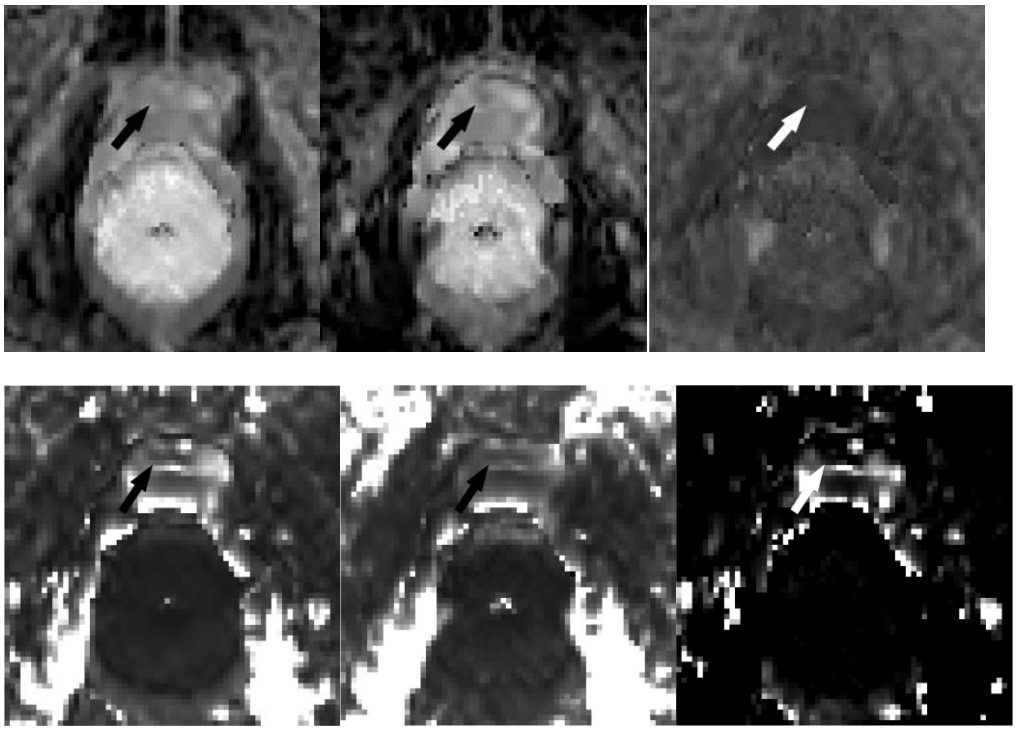

Figure 3.3 ADC map acquired with TE=47 ms (top left) and ADC map acquired with TE=75 ms (top middle) for a patient with Gleason 6 adenocarcinoma (black/white arrow). A subtraction image of the two (ADC(TE=75 ms) – ADC(TE=47ms)) was generated to demonstrate the effect of TE on ADC of a Prostate cancer focus compared to normal prostate (top right).. T2 maps generated with b=0 s/mm^2 (left) and b=750 s/mm^2 (middle) are shown on bottom. A subtraction image of the two T2 maps (T2(b=0 s/mm^2) – T2(b=750 s/mm^2)) was generated (bottom right). Window and level was adjusted independently for each image.

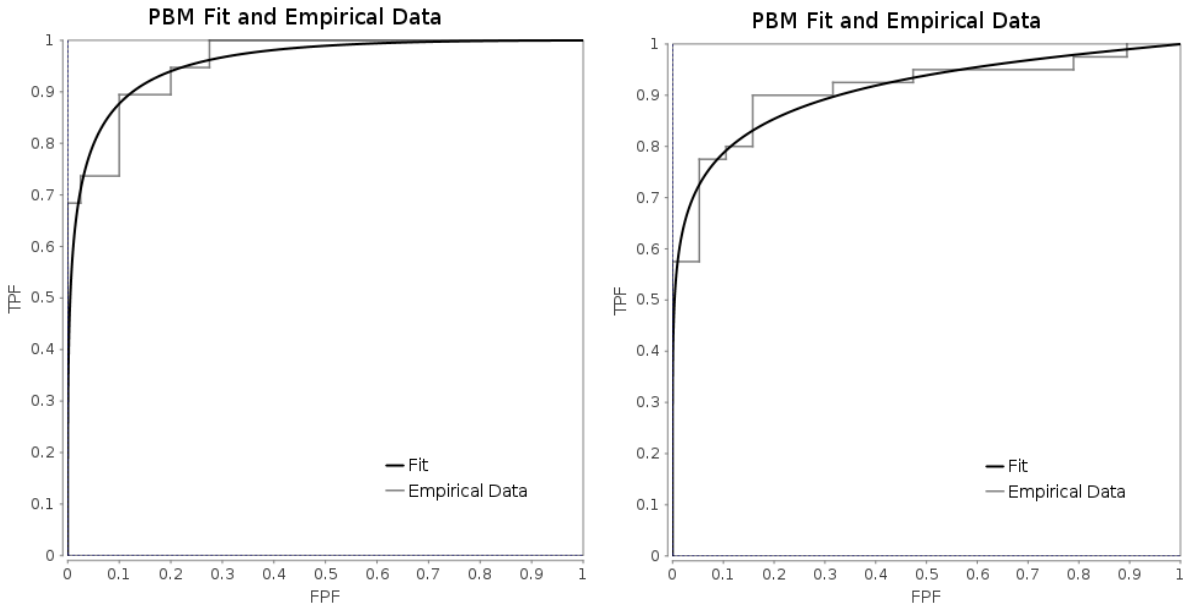

Figure 3.4 ROC curve for LDA-derived data classifier (left) vs. baseline ADC alone (right) in differentiating between normal and cancerous ROIs. The baseline ADC was acquired with a TE of 47ms, representing the clinical standard. The LDA-derived classifier includes information relating to not only this ADC(TE=47 ms) but also ADC(TE=75 ms), ADC(TE-100 ms), T2(b=0 s/mm^2) and T2(b=750 s/mm^2). The AUCs were 0.96 and 0.91, respectively.

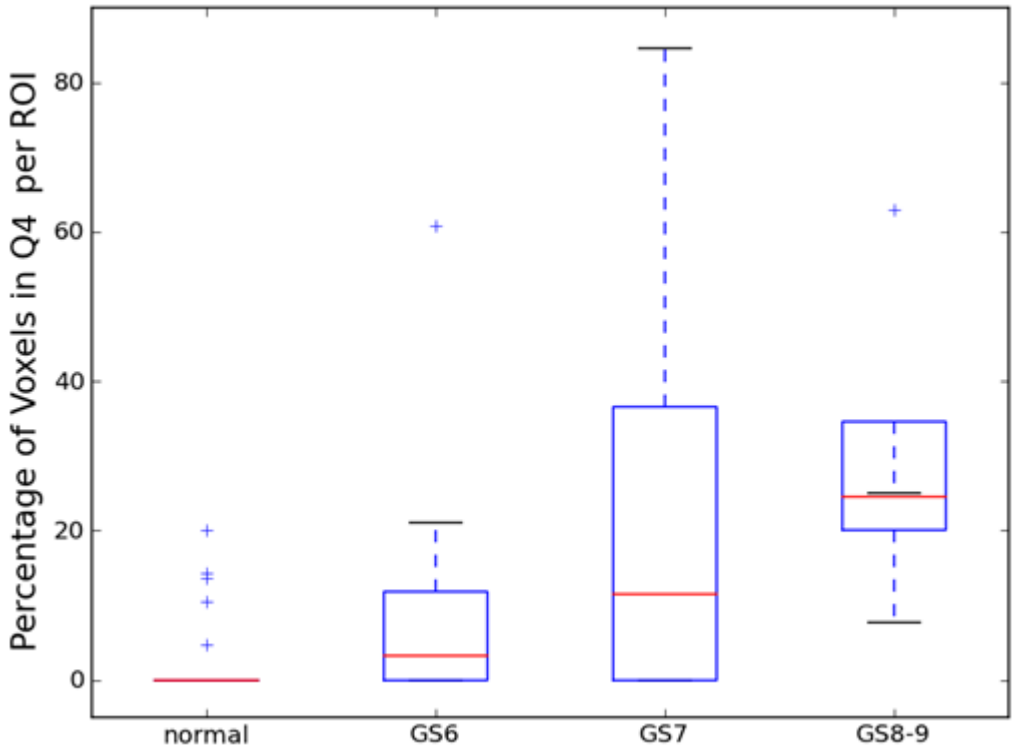

Figure 3.5 Boxplot showing PQ4, the parameter describing the percentage of voxels within Quadrant IV (lower right) of Figure 1, as a function of Gleason score. This quadrant corresponds to an increased T2 with increased b-value and decreased ADC with increased TE. Red lines represent the median value of the parameter, boxes extend to the 25^{th} and 75^{th} quartiles and crosses represent outliers. The trend had a Spearman coefficient of $\rho=0.508$ indicating a significant linear trend, with $p=2.5\times10^{-5}$, with $p<0.0001$.

3.4 Discussion

Our results show that the mean ADC in normal prostate increases more than the mean ADC in cancer when TE is increased from 47 ms to 75 ms. The mean T2 of normal prostate decreases more than the mean T2 of cancer with increasing b value. These findings suggest that ADC at TE=75 ms may be diagnostically more useful than ADC at TE=47 ms, the current clinical standard (figure 3.3) and that interdependence of T2 and ADC can be used to improve diagnosis of Prostate cancer.

We hypothesize that the changes in ADC and T2 with increasing TE and b value, respectively, are related to the microanatomy of the tissue. Normal prostate tissue has a prominent glandular structure with a large volume of glandular lumen. The free fluid in the lumen has a long T2 and high ADC (76). The glandular lumen is surrounded by glandular epithelium and stromal tissue. Water in the epithelium and stromal environment has a relatively short T2 and a lower ADC compared to lumen. As TE is increased, the contributions to ADC from the epithelium and stroma should be reduced, resulting in an increased ADC approaching that of the isolated lumen. Conversely, as b value is increased, signal from tissue with a high ADC, i.e., lumen, should be diminished. The measured T2 thus would approach the lower T2 of stroma. A large increase in ADC with increasing TE, and a large decrease in T2 with increase in b value suggests a large fractional luminal volume, and therefore decreased probability of cancer (77). We hypothesize that hybrid imaging could provide quantitative estimates of luminal fraction by measuring these changes relative to estimated ADC and T2 of luminal fluid and stroma.

Prostate cancer is marked by a decreased percentage of glandular lumens and a dense cellular structure with a short T2 and low ADC relative to lumen. This is more prominent with aggressive cancers; as Gleason score increases, the luminal volume decreases (78). Without a large luminal volume, the signal contributions should not change when b is increased and T2 remains approximately constant.

In addition, our results suggest that a small but significant component of cancers is characterized by increasing T2 with increasing b value, and decreasing ADC with increasing TE. This suggests the presence of an environment in cancers with restricted diffusion (low ADC) and a long T2. This signal determines the value of the 'PQ4' parameter introduced here. A high PQ4 may reflect the intracellular water signal from the cytoplasm or nuclei of cancer cells (79-80) where diffusion of water is restricted, and perhaps a larger fraction of mitotic cells in cancers associated with increased T2 (81-4). Virtually all of the pixels in quadrant 4 of figure 3.1 are from cancers (hence a high 'PQ4'), while almost all voxels from normal prostate appear in quadrant 2 (low 'PQ4'). A high value of PQ4 suggests a lower percentage of water in a luminal environment, and a higher percentage of water in a restricted environment with long T2. Therefore, 'PQ4' shows promise in differentiating between normal and cancerous tissue with different glandular structures by encapsulating the dependence of T2 and ADC on b and TE, and changes in underlying histology consistent with cancer. Conventional approaches that measure T2 and ADC independently cannot detect these effects. PQ4 is fundamentally different from T2 and ADC and therefore may provide independent diagnostic information that increases diagnostic accuracy when used in combination with ADC and T2.

The LDA classifier improved Prostate cancer detection relative to ADC at TE=47 ms alone, although we were unable to demonstrate statistical significance of the increased AUC. We hypothesize that limitations in sample size and lack of an independent testing database limit the statistical power. Nevertheless, this result suggests that the additional information included in the hybrid data matrix due to sampling at multiple combinations of TE and b values can increase diagnostic accuracy.

The heterogeneous nature of Prostate cancer can make it difficult to detect when cancer foci are distributed amongst normal glands, even when quantitative methods are used. Langer et al. evaluated T2 and ADC in sparse and dense Prostate cancer PZ tumors which they defined as containing greater than or less than 50% primarily normal PZ tissue, respectively. They reported no significant difference between ADC or T2 of sparse prostate tumors and normal PZ tissue concluding that MRI may be limited for Prostate cancer detection and tumor volume assessment in sparse cancers (85). Our hybrid imaging technique may be able to better assess such tumors when used in conjunction with ADC and T2 alone by isolating the cancerous component from the normal glands based on the response of ADC and T2 to changing TE and b value. This is particularly important in low grade tumors where physicians and patients must decide on treatment or active surveillance, and for localization for focal therapies or targeted biopsy.

The small sample size (n=21) of the patient cohort is a limitation of this study. In particular, only a small number of high grade (Gleason 8, 9) cancers (n=4) satisfied inclusion criteria. A future study with a significantly increased number of patients and high grade cancers is necessary to more accurately assess the correlation of PQ4 and

other hybrid parameters with Gleason score, and evaluate the morphology of high grade cancers in hybrid images. Due to limitations on the time available for data acquisition, higher b values were not investigated in this study. Development of accelerated hybrid methods in the future will allow sampling of more combinations of b and TE values with a realistic acquisition time. The study of patients who later received a radical prostatectomy introduces a patient selection bias into the study. Histological analysis of prostatectomy specimens is the gold standard for Gleason score assignment and cancer localization so this bias is unavoidable. The method of correlating cancers on T2W images or ADC maps with histology may introduce bias in the evaluation of parameters derived from ADC and T2 (e.g. PQ4). However, our primary goal was *not* to accurately measure sensitivity and specificity of hybrid parameters but *rather* to evaluate the characteristics of new hybrid parameters in regions that are identified as cancer on histology. The diagnostic performance of hybrid imaging in a blinded setting is beyond the scope of this pilot study. Lastly, the study was confined to a single center with all imaging performed at our institution.

3.5 Conclusion

In conclusion, hybrid T2-diffusion-weighted MR imaging shows promise for improved diagnosis of prostate cancer and for determining its aggressiveness. Hybrid imaging produces maps of the changes in ADC and T2 with changing TE and b values. These changes in each voxel are likely determined by the histological structure of the tissue. In prostate, this is heavily influenced by luminal volume, an important marker for

cancer aggressiveness. In addition, hybrid MRI identifies a population of water molecules with restricted diffusion and long T2 that is associated with cancer.

CHAPTER 4

EXTENSION OF HYBRID IMAGING METHODOLOGY TO T1-T2 IMAGING

In Chapter 3, I described a hybrid T2-DW imaging method for prostate cancer diagnosis and determination of aggressiveness. The results of that study suggest the presence of a compartment in prostate cancer which has a long T2 and restricted diffusion. In this chapter, I extend the hybrid methodology to T1-T2 imaging. This pilot study is a proof–of-concept for hybrid T1-T2 imaging on a limited patient data set. I present here image features of normal prostate tissue, pathologically proven cancers, Benign Prostatic Hyperplasia (BPH), and other prostatic abnormalities based on hybrid T1-T2 images which may be useful in the future for distinguishing prostate cancers. A full analysis of the diagnostic capabilities of a hybrid T1-T2 approach and its efficacy compared to a hybrid T2-DW approach is beyond the scope of this dissertation.

4.1 Introduction

Multiparametric MRI (mp-MRI) has become a powerful tool in non-invasive imaging of prostate cancer. As discussed in Chapter 2, T2-weighted imaging and DW-MRI make up the core of a standard mp-MRI exam (86). T1-weighted imaging has been primarily limited to use with an intravenous contrast agent for Dynamic Contrast Enhanced MRI (DCE-MRI) (86-7).

Recent reports of Gadolinium retention in bone and brain tissue following as low as a single DCE-MRI exam have raised concerns over the use of gadolinium-based contrast agents (88-91). Although the concentrations detected are very low, gadolinium in its unchelated form is toxic and these reports warrant further study. A recent publication further found that retention was not limited to group 1 agents, which are considered of higher risk of the gadolinium breaking away from the chelate and are not as commonly used; retention in both bone and brain was present in patients who had been administered solely a group 2 agent, which have been generally considered safer (92-3).

Patients with low kidney function are also at risk of developing Nephrogenic Systemic Fibrosis (NSF) from the injection of gadolinium based contrast agent (94-6). These patients may not be able to tolerate a standard DCE-MRI exam. Finally, parameters extracted from DCE-MRI have been reported to overlap between BPH and cancers due to increased microvessel density in BPH (97-8). These concerns have prompted increased interest in non-contrast agent imaging methods.

One way to exploit differences in T1 relaxivity in prostate MRI without the need for contrast agent injection is to detect the dependence of measured T1 on TE. This methodology hinges on the work presented in Chapter 3. Our results from that study suggest the existence of multiple compartments of water molecules within the prostate tissue including a compartment with long T2 in a restricted diffusion environment which is present in prostate cancer. These compartments all contribute to detected signal within a voxel. Using a hybrid approach to manipulate these signal contributions may allow us to better identify cancer foci and Gleason Score.

Similarly to the inherent interdependence of T2 and ADC utilized in hybrid T2-DW MRI, T1 and T2 relaxation occur simultaneously and differences in these relaxation times between different environments affect each other's measurements.

A typical T1-weighted scan minimizes T2 relaxation by setting the TE to be very short. The protons then have minimal time to dephase before readout. A typical T2-weighted scan uses a long TR to allow recovery of the longitudinal magnetization and minimize dependence on T1. The signal measured using a spin echo sequence and ignoring contributions from diffusion, which was discussed in Chapter 3, is given by,

$$S = S_0 e^{-\frac{TE}{T2}}(1 - e^{\frac{TR}{T1}})$$

where S_0 is a constant, representative of the signal prior to any dephasing or relaxation. Setting a short TE will minimize the first exponential term so that the T2 effect on measured signal can be assumed negligible, giving

$$S = S_0(1 - e^{\frac{TR}{T1}})$$

Similarly, setting the TR to be short will minimize the second exponential term so that the T1 relaxation effects are diminished, resulting in,

$$S = S_0 e^{-\frac{TE}{T2}}$$

In this study, we present a hybrid T1-T2 MRI approach in which we image at multiple TEs and multiple TRs and detect the response of T1- and T2- based parameters to changing TE and TR, respectively. Based on the results of the study presented in Chapter 3, we hypothesize that distinct populations of water molecules with characteristic T1-T2 pairings will respond differently to changing TE and TR. Some

of these compartments may be emphasized in cancer. The purpose of this study is to assess the feasibility of an investigation into hybrid T1-T2 imaging for prostate cancer diagnosis. We are not attempting to assess the diagnostic accuracy or benefit of hybrid T1-T2 imaging at this point.

4.2 Materials and Methods

4.2.1 Patients

Fourteen patients receiving a clinical, diagnostic prostate MRI through the Department of Radiology at our institution between January and August 2015 were included in this study. This study was Health Insurance Portability and Accountability Act compliant. All patients either had, or were scheduled for, a transrectal ultrasound-guided biopsy. 3 out of 14 patients received a radical prostatectomy following the MRI exam. Each patient recruited for this study received a standard mp-MRI, clinical exam consisting of: T2 weighted turbo spin-echo (TSE) sequences, T1 weighted TSE sequence, T2 mapping, DCE-MRI sequence and a hybrid T1-T2 sequence. All images were acquired with free breathing on a Philips AchievaTX 3 Tesla scanner (Philips Healthcare, Best, Netherlands) using a combination of an endorectal coil (Medrad, Bayer Healthcare, Warrendale, PA) and a 6-channel, cardiac, phased array coil placed around the pelvis. Each patient received an intramuscular, 1 mg dose of Glucagon (Glucagon, Lily, Indianapolis, IN) immediately preceding the MRI exam to prevent peristalsis of the rectum.

4.2.2 Hybrid MRI Sequence

The T1-T2 hybrid sequence consisted of four, standard, TSE sequences with a combination of 2 TEs and 2 TRs: TE/TR= 80 ms/2,800 ms, 80 ms/10,000 ms, 220 ms/2,800 ms and 220/10,000 ms. The turbo factor was lowered to eight so that differences in TE across k space were minimal. The T1-T2 sequence is described in Table 1. Images were acquired in the axial plane with the FOV oriented perpendicular to the rectal wall. Fat saturation was not used. The hybrid imaging took place before the injection of Gadolinium and any dynamic imaging.

4.2.3 ROI Delineation

Following the MRI exam, Regions of Interest (ROIs) were identified and defined by a radiologist (Serkan Guneyli, 10 years of experience in prostate MR imaging) based on biopsy or prostatectomy specimen histology. Patient characteristics are listed in table 2. The radiologist first read all relevant biopsy or prostatectomy pathology reports as well as the radiology report. If cancer was reported in the histopathology and apparent on MRI, it was outlined on the clinical ADC map or T2-weighted image using the PACS interface (iSite, version 3.6.150, Philips Healthcare). If biopsy reports were normal for a particular sextant and there were no abnormalities visible on the MRI, a normal ROI was drawn. If a region looked very suspicious on MRI and was reported as suspicious on the

Table 4.1 T1-T2 hybrid scan parameters

TE	80 ms, 220 ms
TR	2.8 s, 10 s
In plane resolution	0.313 mm x 0.313 mm
Matrix size	448 x 448
Slice thickness	3 mm
Number of Slices	20
Turbo factor	8
NEX	2
Scan time	13 minutes

radiology report but biopsy cores came back negative for cancer, it was outlined on MRI and labeled as suspected cancer. Lastly, Benign Prostatic Hyperplasia (BPH) was outlined in the Transition Zone (TZ) if pathologically proven. From the 14 patients, 11 confirmed cancer ROIs, 5 BPH nodules, 23 normal ROIs and 9 suspected cancer ROIs were defined. In addition, 2 cases of extensive Prostatic Intraepithelial Neoplasia (PIN) were identified and delineated.

After ROIs were delineated on the PACS interface, they were transferred to the hybrid image set semi-automatically using 3D Slicer (7). This was performed assuming no motion or deformation between scans. Scans with ROIs overlaid were visually inspected for accuracy. No obvious misalignment was visually apparent.

Table 4.2 Patient Characteristics

Patients	n=14	Cancer rois	n=11
Patients with pathology-proven cancer	n=8	Normal rois	n=23
Patients with only suspected but not pathology-proven cancer	n=3	Suspected cancer rois	n=9
Patients with pathology-proven and suspected but not proven cancer	n=2	BPH rois	n=5
Patients without cancer	n=3	Other abnormalities rois	n=2
		Total rois	N=50

Data was filtered to exclude corrupt voxels, which were not included in the analysis. The voxels were considered corrupt if either of the TE=80 ms data points' signal intensity were less than a threshold value. The threshold was chosen to correspond with a necessary SNR of at least 6.7, or NSR of 15%. This implies that the minimum, meaningful change in signal intensity which we would be able to measure is 15%. Noise was determined using the standard deviation of an ROI drawn in the filled

bladder. The ROI size was predefined and chosen to be comparable to the average prostate ROI. The ROI was placed by the user and propagated to the two surrounding slices. This geometry was chosen to minimize structural variability and sensitivity to coil proximity. This was repeated four times for each patient with different ROI placement. The minimum standard deviation within the ROI was then assigned as the threshold for each patient, and each image. This was performed using custom software written in Matlab (Mathworks, Natick, MA).

4.2.4 Data Analysis

The hybrid imaging sequence results in a 2x2 imaging array. This sampling is too sparse for confident T1 and T2 calculations. Instead, we computed ratios of signal at different parameter combinations. The ratios, and calculated differences in ratios, are defined as:

$$RTR(TE = 80ms) = \frac{S(TE = 80\,ms,\ TR = 2.8\,s)}{S(TE = 80\,ms, TR = 10\,s)}, \quad RTR \in [0,1]$$

$$RTR(TE = 220ms) = \frac{S(TE = 220\,ms,\ TR = 2.8\,s)}{S(TE = 220\,ms, TR = 10\,s)}, \quad RTR \in [0,1]$$

$$RTE(TR = 2.8s) = \frac{S(TE = 220\,ms,\ TR = 2.8\,s)}{S(TE = 80\,ms, TR = 2.8\,s)}, \quad RTE \in [0,1]$$

$$RTE(TR = 10s) = \frac{S(TE = 220\,ms,\ TR = 10\,s)}{S(TE = 80\,ms, TR = 10\,s)}, \quad RTE \in [0,1]$$

$$\Delta RTR = RTR(TE = 220\,ms) - RTR(TE = 80\,ms), \quad \Delta RTR \in [-1,1]$$

$$\Delta RTE = RTE(TR = 10\,s) - RTE(TR = 2.8\,s), \quad \Delta RTE \in [-1,1]$$

where S is the signal within a given voxel. All ratio calculations were done on a voxel-by-voxel basis.

To quantify the presence of patterns in ΔRTR corresponding to changes in T1 with increasing TE, we analyzed the percentage of voxels displaying these patterns. We are interested in voxels which have a substantial change in RTR. Based on the reasoning presented in 4.2.3 regarding data filtration, we chose that change (negative or positive) to be 0.15. For each ROI we calculated the percentage of total voxels within the ROI which showed a greater than 0.15 increase in RTR with increasing TE.

A paired Students t test was used to compare RTR(TE=80ms) and RTE(TE=220ms) for both normal PZ and pathologically-proven cancerous ROIs. An unpaired Student's t test was used to compare ΔRTR and ΔRTE between normal PZ and pathologically-proven cancerous ROIs. The percentage of voxels with ΔRTR>0.15 within an ROI was compared between normal PZ and pathologically proven cancers using an unpaired Students t test.

4.3 Results

Patient images of cancerous and normal ROIs are shown in figure 4.1 and figure 4.2. The mean and standard deviation of change in RTR with increasing TE were -0.03 ±0.29 for pathology-proven prostate cancer and -0.07 ± 0.19 for normal PZ tissue ($p<0.05$). The mean and standard deviation of change in RTE with increasing TR was -0.01 ± 0.15 for prostate cancer and 0.05 ± 0.06 for normal PZ ROIs ($p<0.05$). The percentage of total voxels within an ROI which had an increase in RTR of greater than

0.15 was 27% ± 9.6% for pathologically-proven cancers and 8.4% ± 15% for normal PZ tissue ($p<0.05$) (figure 4.3). For no pathologically-proven cancer ROIs or suspected cancer ROIs was this value 0%. In contrast, 9 out of 23 normal PZ ROIs had 0 voxels with $\Delta RTR>0.15$.

Table 4.3 Voxel based values across all patients, mean +/- standard deviation; RTE, RTR Є [0,1], ΔRTR, ΔRTE Є [-1,1]

	RTE (TR=2.8)	RTE (TR=10)	RTR (TE=80)	RTR (TE=220)	ΔRTE	ΔRTR
Cancer	0.2 ± 0.14	0.19 ± 0.15	0.81 ± 0.14	0.78 ± 0.26	-0.01 ± 0.15	-0.03 ± 0.29
Normal	0.49 ± 0.14	0.54 ± 0.17	0.84 ± 0.12	0.77 ± 0.17	0.05 ± 0.16	-0.07 ± 0.19
Suspected	0.19 ± 0.14	0.19 ± 0.15	0.79 ± 0.14	0.75 ± 0.29	0.00 ± 0.16	-0.04 ± 0.31
BPH	0.29 ± 0.16	0.31 ± 0.17	0.8 ± 0.13	0.74 ± 0.25	0.02 ± 0.14	-0.06 ± 0.27
Other	0.31 ± 0.16	0.3 ± 0.09	0.69 ± 0.18	0.67 ± 0.2	-0.01 ± 0.18	-0.02 ± 0.23

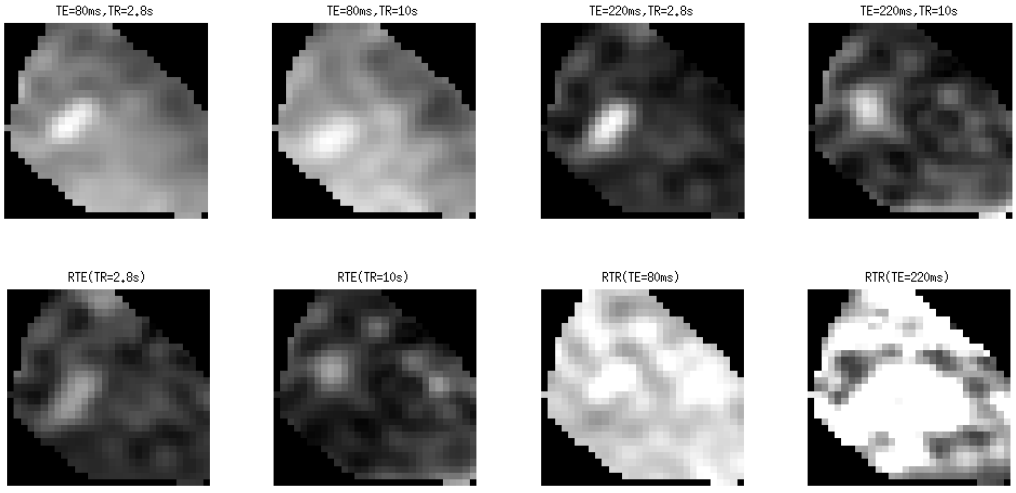

Figure 4.1. T1- and T2-weighted images (top) of a biopsy-proven cancer focus and corresponding ratio maps (bottom). The entire ROI, and only the ROI, is shown.

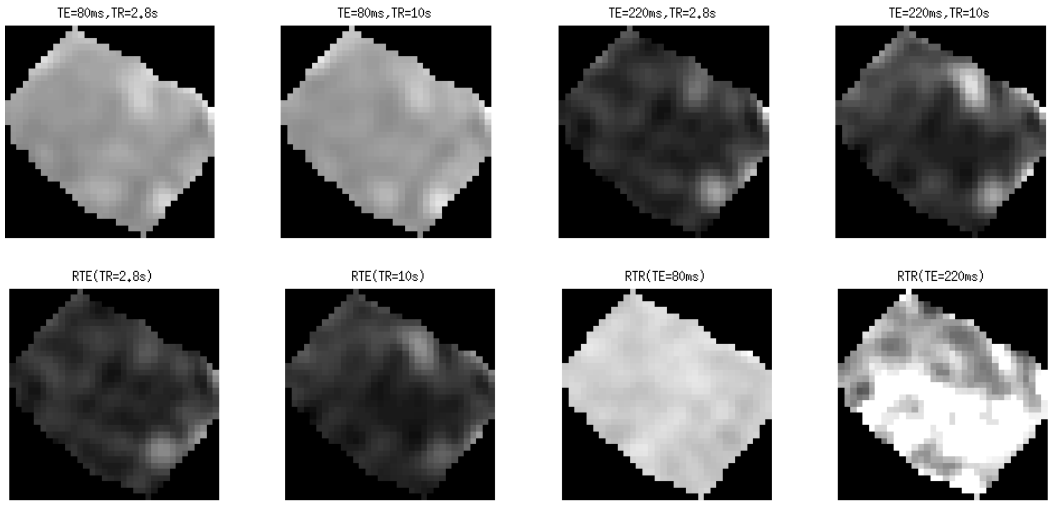

Figure 4.2 T1- and T2-weighted images (top) of a biopsy-proven cancer focus and corresponding ratio maps (bottom). The entire ROI, and only the ROI, is shown.

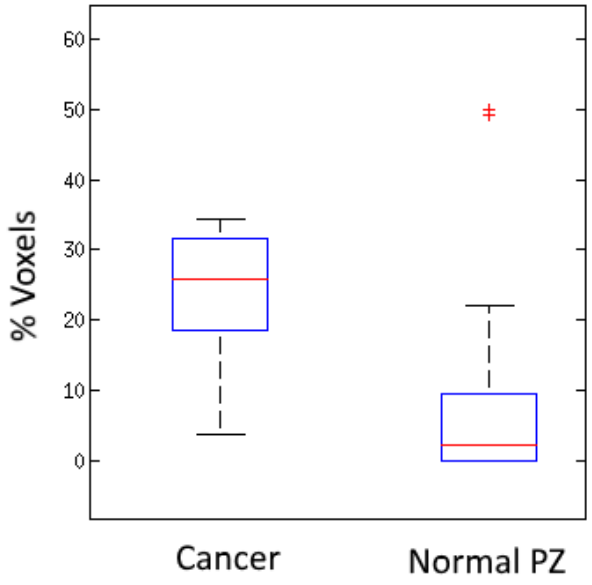

Figure 4.3 Boxplot showing the percentage of total voxels within an ROI with a greater than 0.15 increase in RTR with increasing TE (ΔRTR>0.15) for normal PZ ROIs (n=23) and pathologically-proven cancers (n=11).

4.4 Discussion

Our results show that on average RTR and RTE do not change very much in response to changing TE and TR. RTR shows a greater range of changes, however, in pathologically-proven cancer than in normal PZ tissue. This suggests that cancer foci have a heterogeneous response to changing TE. In particular, we see a large component of cancers compared to normal PZ tissue with a greater than 0.15 increase in RTR (decrease in T1) when we increase TE. This is consistent with a large luminal volume in normal PZ tissue.

Normal PZ tissue contains a large volume of luminal fluid in the ducts. This will have a long T1 and T2. Increasing TE should, therefore, not give a large change in T1. Increasing TR should not change T2 much. The long T1, long T2 coupling of the luminal fluid likely dominates the signal at short TE and short TR. As TE and TR are increased, this pattern remains dominant. Cancer tissue has a lower number and volume of lumen. Contributions from the stromal and epithelial tumor environment give a lower measured signal at short TE and TR. At higher TE, signal contributions from short T2, short T1 components in the epithelium and stroma are likely reduced. An increase in RTR, and thus decrease in T1, suggests the presence of a compartment with longer T2 and shorter T1 than these components.

The multiple compartments of prostate tissue with different T1s and T2s are known to exist and the effect of this multiplicity on MRI-based parameters has been studied by multiple groups. Langer et al. correlated MR parameters to histological features for 24 prostate patients with pathologically proven Gleason 6 and 7 prostate

cancers (99). They looked at DWI, DCE-MRI, T2-weighted images and T2 maps with all imaging performed at 1.5T with an endorectal coil and a cardiac phased array coil. They correlated image-based parameters with histology-derived parameters, i.e., the percentage volume of different tissue components. They measured ADC, T2, K^{trans} and extravascular, extracellular space, v_e. They calculated the percentage of nuclei, cytoplasm, stroma and luminal space using image segmentation from whole mount pathology.

This study found that ADC and T2 were negatively correlated to percentage area of nuclei and of cytoplasm and positively correlated with luminal space. This is consistent with our results. Neither parameter was significantly related to percentage area of stroma. On the other hand, K^{trans} decreased significantly as percentage area of lumen increased. K^{trans} also showed a negative correlation with percentage area of stroma. Percentage area of nuclei and of stroma were significantly correlated with v_e.

Additionally, looking at the histological properties of the prostate cancers and normal PZ tissue, cancers had significantly higher percentages of nuclei and cytoplasm (23.7% vs. 14.5% and 22.5% vs 16.7%, respectively) and lower percentage of luminal space than normal prostate (13.5% vs. 29.6%). This is consistent with our results showing a large percentage of cancerous voxels with an increase in RTR with increasing TE. Langer also notes that increased nuclear size and cellular density may also be indicative of benign conditions including PIN. This may be reflected in our high measured RTE and low measured RTR values in PIN. As presented in Chapter 3, results of our previous study suggested the presence of a long T2, restricted diffusion environment in prostate cancer which we theorize could be caused intracellular water. It

is possible that this environment relates to enlarged nuclei and has a low T1 (and thus RTR).

T1 and T2 may also be affected by cell cycle in prostate cancer. Rapidly growing cancers will contain more cells undergoing mitosis than normal PZ tissue. The intracellular environment and prevalence by volume of this environment will change during stages of the cell cycle. Callahan et al. looked at the T1 and T2 relaxation times of cells as a function of cell cycle (83). Experiments were performed at 7T (300 MHz). He found that T1 was invariant with regard to cell cycle, and T2 depended on cell cycle phase. Following the administration of Epidermal Growth Factor (EGF), T1 stayed at 2.2-2.5 seconds and T2 varied between 0.065 and 0.15 seconds. He concluded that T1 appeared to be insensitive to changes in physiology that affected T2. T1 is very sensitive to changes in hydration; however, water content has been measured to be stable throughout the cell cycle. T2 of intracellular water is, on the other hand, affected by processes such as chemical exchange of protons macromolecules and hydration water, and molecular diffusion of water through internal field gradients as well as exchange diffusion of water between bulk and hydration water regions.

De Certaines et al. published a study in which T1 and T2 times were measured over 48 hours in regenerating rat liver following partial hepactomy (84). The results showed that T1 was relatively constant but T2 showed a 30% change in regenerating liver compared to control. They also found that T1, but not T2, showed fluctuations following circadian patterns. This was reported previously to be a dramatic change (60% T1 increase) in tumor cells. It is further noted that changes in T1 and T2 in tumor cannot be explained solely by water content. The biological factors leading to changes could be

cell division and differentiation loss. Beall et al. showed in synchronized HeLa cells that T1 is maximized during mitosis and is minimal during the S phase (81). It was hypothesized that T1 is increased by spermine chromatin condensing.

Another approach to sensitizing T1 or T2 estimates to multiple compartments within prostate tissue is to perform a multiexponential T1 or T2 analysis, corresponding to a two compartment model with a fast T1 or T2 compartment and a slow T1 or T2 compartment. Storas et al. published a study on bi-exponential fitting of prostate T2 imaging (100). They found that the bi-exponential short T2 was 64 msec (range 43 to 92 msec) and the long T2 was 490 msec (range 161 to 1319 msec). The fitted signal fraction, f, of the long T2 component was 27% (range 3% to 80%). Multi-exponential diffusion behavior has also been observed in BPH by Kershaw et al. (98) and by Kjaer et al (101). Limitations of this approach to evaluating tissue in terms of multiple compartments is that multiple compartments may exist which have similar T2s but different T1s. A multi-exponential T2 would not be able to detect these where a hybrid approach may be able to. We believe that this makes a hybrid approach possibly more sensitive to histopathological differences between normal PZ tissue and prostate cancer.

Changes in epithelial, stromal and luminal volume and structure have been shown to correlate with Gleason score (102). Our hybrid T1-T2 imaging method may increase sensitivity to the relative volumes of these compartments. Gleason scores are available for the patients imaged in this study but we considered an analysis of hybrid imaging-based parameters for different Gleason scores beyond the scope of this study. This was for two reasons: sample size and reference standard. We defined ROIs based

on histology reports primarily of biopsy cores (unless prostatectomy specimen histology reports were available). Gleason scores assigned based on biopsy results may be unreliable (see 1.2.2). The gold standard for Gleason score assignment and ROI delineation on imaging is correlation of imaging with prostatectomy specimen histology. A future analysis of hybrid T1-T2 imaging-based parameters and correlation with Gleason score would benefit from a collaborative ROI delineation process with a pathologist and radiologist. Not only would this allow for an accurate assessment of hybrid T1-T2 image-based parameters with Gleason score, but it is also probable that variation in hybrid-based parameters amongst cancerous ROIs in our study is partially due to the multiple Gleason patterns included.

It should be emphasized that our study is limited in its number of patients and pathologically confirmed cancers. We present here a demonstration of features obtained from a novel imaging approach. We are not trying to evaluate the diagnostic ability of such an approach. That is beyond the scope of this study and would require a much greater number of patients. We are only presenting our experience regarding the feasibility of investigating an approach such as this. It may be of curiosity to the reader that we have presented an investigation of T1-T2 hybrid imaging, thinking this to be redundant of results of our previous hybrid T2-DW MR analysis. However, we note that hybrid T1-T2 imaging could identify compartments which have similar T2 and ADC pairings, but different T1s and therefore would be indistinguishable using hybrid T2-DW imaging. Additionally, DW-MRI can be especially prone to motion and artifacts caused by eddy currents (see 1.4.4). It is possible that using T1 and T2 rather than T2 and DW-MRI in a hybrid acquisition could be advantageous for artifact reduction.

Future evaluation of the proposed T1-T2 hybrid imaging method would benefit from an increased TE and TR sampling. Limited scan time necessitated sampling at only two TEs and two TRs for this initial investigation. Sampling additional TEs and TRs would allow for proper calculation of T1s and T2s. It is also possible that utilizing a shorter TR could better emphasize differences in T1 at different TEs.

An interesting extension of this work would be to use hybrid T1-T2 MRI in conjunction with contrast agent injection. Incorporating hybrid T1-T2 MRI into DCE-MRI could give information regarding the uptake of gadolinium into different tumor compartments. Quantitative DCE-MRI analysis is currently based on a two-compartment model, but ex-vivo, high resolution imaging suggests that gadolinium migrates into the prostatic ducts (103). Hybrid T1-T2 imaging could utilize differences in T2 of different environments to emphasize gadolinium concentrations present in those different environments. Theoretically, this could increase sensitivity and perhaps allow for a lower dose of contrast agent.

In conclusion, a hybrid T1-T2 imaging method may provide additional information which complements traditional mp-MRI regarding tumor structure. Hybrid MRI has the potential to identify multiple compartments of water molecules within prostate, some of which may be indicative of prostate cancer. We have previously demonstrated this concept using T2 and DW-MRI. We extend the hybrid methodology here to T1 and T2 imaging to emphasize different compartments with distinct combinations of T1 and T2. Our results suggest that further investigation into the diagnostic ability of a T1-T2 hybrid imaging approach is warranted.

CHAPTER 5

CONCLUSION

I have presented here an evaluation of a multidimensional, hybrid MR imaging concept in prostate cancer. This imaging method samples a series of scan parameters (TE, TR, b value) and detects differences in T1, T2 and ADC to identify or emphasize subvoxelar populations of water molecules with specific parings of T2 and ADC or T1 and T2. The presence of specific compartments of water molecules may be indicative of prostate cancer. In prostate cancer, the most pronounced structural feature is reduced glandular luminal volume and restricted intercellular diffusion due to a dense cellular structure. These differences become more pronounced with increasing Gleason Score. Hybrid MRI is sensitive to these and other changes in tissue structure, making it a potential method for future noninvasive determination of prostate cancer aggressiveness.

In Chapter 2, I established the short-term reproducibility of ADC in normal prostate tissue and prostate cancer. I evaluated back-to-back DW-MRI scans taken while the patient remained on the table with only automatic tuning and matching performed in between. I found that ADC variation within the prostate is reasonable, on the order of 10%, and lower than those reported for other abdominal organs. I did not find variation in ADC to vary significantly with location within the prostate, which is important for the potential use of DW-MRI for localization of biopsy needle placement or focal therapy guidance.

This study evaluated short-term reproducibility representing the minimum variation in ADC inherent to the imaging procedure. This is likely due to variability of physiological processes in the tissue and cannot be mitigated by changing scan parameters or setup. Now that the minimum possible variability of ADC in prostate has been established a comprehensive study of additional sources of variability, such as intra-patient and intra-scanner variability, is necessary to fully determine the potential of ADC as a quantitative imaging biomarker.

In Chapter 3, I presented a study on a novel, hybrid, multidimensional T2-DW MR Imaging sequence for prostate cancer. This sequence utilizes the interdependence of ADC and T2 to isolate populations of water molecules within a voxel based on how they respond to both an increasing b value and an increasing TE. In prostatic tissue, these populations correspond to free water in the fluid-filled glandular lumen and bound water in the stromal and epithelial cellular matrix. My results suggested the presence of a compartment of water molecules within prostate cancer with a long T2 in a restricted diffusion environment. Such a compartment has been theorized but never demonstrated before *in vivo*. The prevalence of this compartment was seen to increase with Gleason Score.

The main limitation of this study was sample size. As a pilot study, only 21 patients were enrolled due to limitations on scanner availability and the time consuming nature of the correlative pathology-radiology review of each case. This small sample size did not provide sufficient statistical power to evaluate the diagnostic performance of hybrid T2-DW MRI compared to standard clinical parameters such as ADC alone. As noted, however, the goal of this study was not to perform a full analysis of the diagnostic

capabilities of the sequence. A future study with a large patient enrollment will be necessary. Additionally, the b values used for this study were found to be suboptimal. Despite collecting data at b values of 0, 750 and 1500 s/mm^2, only the b values of 0 and 750 s/mm^2 were used in the analysis. This is due to an interesting result of this particular b value spacing combined with the least squares regression algorithm in which only two b values contribute to the estimated ADC (see appendix). Future studies will benefit from a different b value sampling scheme.

In Chapter 4, I extended the hybrid methodology to T1-weighted and T2-weighted imaging. Using hybrid T2-DW imaging, I was able to identify a compartment within prostate cancer with long T2 and low ADC. With hybrid T1-T2 imaging, it is possible to identify additional compartments that may have unique T1-T2 pairings but not T2-ADC pairings. I found that when TR and TE were increased, the mean difference in T2 and T1 related parameters was close to zero. However, tumors tended to respond more heterogeneously than normal prostatic tissue. This study is a proof-of-concept which seeks to determine the characteristics of hybrid T1-T2 images in prostate cancer and normal prostate tissue. In the future, it may be of interest to use hybrid T1-T2 imaging in conjunction with contrast injection to incorporate time-dependent perfusion information.

Sample size was again a limitation in this study. This evaluation was intended to demonstrate the potential of a T1-T2 hybrid MRI imaging sequence, not evaluate the diagnostic ability of hybrid T1-T2 imaging. Biopsy was the reference standard for this study, which limited the number of proven cancers and restricted ROI delineation to lesions that were visible on MRI.

In conclusion, my work presented here suggests that using hybrid imaging to identify differences in tissue structure could lead to better differentiation between normal tissue, aggressive prostate cancer and benign tumors or conditions. Hybrid imaging provides structural information undetectable using conventional mp-MRI. It may therefore provide independent, diagnostic information that compliments ADC, T1 or T2 values and increase diagnostic accuracy when used in combination with conventional mp-MRI.

Additionally, differences in geometric acquisition parameters between sequences in mp-MRI make registration difficult. Long acquisition times for DW-MRI often necessitate decreasing spatial resolution and field of view relative to that of T2-weighted imaging. This may cause differences in slice positioning. Artifacts, such as those caused by eddy currents from large DW-MRI diffusion gradients, and motion between sequences further complicate registration. This limits the clinical utility of mp-MRI when attempting to identify voxels that display multiple characteristics of prostate cancer on different MRI sequences. This is particularly problematic for quantitative analysis, where misregistration may lead to spurious parameter estimates. Furthermore, mp-MRI is being increasingly used for focal therapy planning where accurate registration is necessary to deliver targeted treatment with sufficiently small margins. Using hybrid imaging would obviate the need for significant registration and eliminate distortion between scans.

The hybrid MRI methodology investigated here could be adapted to cancers outside of the prostate and to benign prostatic conditions affecting nearly all men during

their lifetime. These conditions can severely affect quality of life but suffer from insufficient diagnostic methods.

To fully evaluate the potential diagnostic ability and accuracy of a hybrid MR imaging method, a study in which quantitative imaging parameters are correlated with quantitative histopathology would be extremely valuable. In the future, a hybrid MRI sequence incorporating T1-, T2- and diffusion weighting could yield even more information regarding tissue structure. Hybrid MRI may provide image-based biomarkers that correspond to structural markers of prostate cancer on the cellular level. If so, hybrid MRI has the potential to noninvasively assess aggressiveness of prostate cancer, which would help reduce over-diagnosis and over-treatment as well as reduce biopsy rates.

REFERENCES

1. Denmeade, Samuel R., and John T. Isaacs. "A history of prostate cancer treatment." *Nature Reviews Cancer* 2.5 (2002): 389-396.

2. National Cancer Institute. Surveillance, Epidemiology and End Results. 2015.

3. Gosselaar, Claartje, Monique J. Roobol, and Fritz H. Schröder. "Prevalence and characteristics of screen-detected prostate carcinomas at low prostate-specific antigen levels: aggressive or insignificant?." *BJU international* 95.2 (2005): 231-237.

4. Gleason, Donald F. "Classification of prostatic carcinomas." *Cancer chemotherapy reports. Part 1* 50.3 (1966): 125-128.

5. Epstein, Jonathan I., et al. "The 2005 International Society of Urological Pathology (ISUP) consensus conference on Gleason grading of prostatic carcinoma." *The American journal of surgical pathology* 29.9 (2005): 1228-1242.

6. Pierorazio, Phillip M., et al. "Prognostic Gleason grade grouping: data based on the modified Gleason scoring system." *BJU international* 111.5 (2013): 753-760

7. Sabolch, Aaron, et al. "Gleason pattern 5 is the greatest risk factor for clinical failure and death from prostate cancer after dose-escalated radiation therapy and hormonal ablation." *International Journal of Radiation Oncology* Biology* Physics* 81.4 (2011): e351-e360.

8. Carter, H. Ballentine, et al. "Early detection of prostate cancer: AUA guideline." *The Journal of urology* 190.2 (2013): 419-426.

9. Hoogendam, Arjen, Frank Buntinx, and Henrica CW de Vet. "The diagnostic value of digital rectal examination in primary care screening for prostate cancer: a meta-analysis." *Family practice* 16.6 (1999): 621-626.

10. Smith, Deborah S., and William J. Catalona. "Interexaminer variability of digital rectal examination in detecting prostate cancer." *Urology* 45.1 (1995): 70-74.

11. Pashtan, Itai, Ming-Hui Chen, and Anthony V. D'Amico. "The impact of PSA and digital rectal examination on the risk of prostate cancer specific mortality in men with a PSA level< 2.5 ng/ml." *Cancer epidemiology* 38.5 (2014): 613-618.

12. Thompson, Ian M., et al. "Assessing prostate cancer risk: results from the Prostate Cancer Prevention Trial." *Journal of the National Cancer Institute*98.8 (2006): 529-534.

13. Hugosson J, Carlsson S, Aus G et al. Mortality results from the Goteborg randomised population-based prostate-cancer screening trial. Lancet Oncol 2010;11:725-732.

14. Schröder, Fritz H., et al. "Screening and prostate-cancer mortality in a randomized European study." *New England Journal of Medicine* 360.13 (2009): 1320-1328.

15. Moyer, Virginia A. "Screening for prostate cancer: US Preventive Services Task Force recommendation statement." *Annals of internal medicine* 157.2 (2012): 120-134.

16. Draisma, Gerrit, et al. "Lead times and overdetection due to prostate-specific antigen screening: estimates from the European Randomized Study of Screening for Prostate Cancer." *Journal of the National Cancer Institute*95.12 (2003): 868-878.

17. Welch, H. Gilbert, and William C. Black. "Overdiagnosis in cancer." *Journal of the National Cancer Institute* (2010).

18. Sandhu, Gurdarshan S., and Gerald L. Andriole. "Overdiagnosis of prostate cancer." *Journal of the National Cancer Institute. Monographs* 2012.45 (2012): 146.

19. Brawer, Michael K. "Prostate-specific antigen: Current status." *CA: a cancer journal for clinicians* 49.5 (1999): 264-281.

20. Thompson, Ian M., et al. "Operating characteristics of prostate-specific antigen in men with an initial PSA level of 3.0 ng/ml or lower." *Jama* 294.1 (2005): 66-70.

21. Scattoni V, Zlotta A, Montironi R, Schulman C, Rigatti P, et al. (2007) Extended and saturation prostatic biopsy in the diagnosis and characterisation of prostate cancer: a critical analysis of the literature. Eur Urol 52: 1309–1322. doi: 10.1016/j.eururo.2007.08.006

22. Mufarrij, Patrick, et al. "Pathologic outcomes of candidates for active surveillance undergoing radical prostatectomy." *Urology* 76.3 (2010): 689-692.

23. Siu, Wendy, et al. "Use of extended pattern technique for initial prostate biopsy." *The Journal of urology* 174.2 (2005): 505-509.

24. ARNP, CUNP, et al. "AUA/SUNA White Paper on the Incidence, Prevention and Treatment." (2012).

25. Ekwueme, Donatus U., Leonardo A. Stroud, and Yanjing Chen. "Cost analysis of screening for, diagnosing, and staging prostate cancer based on a systematic review of published studies." *Prev Chronic Dis* 4.4 (2007): A100.

26. Scott, John G., Eric K. Shaw Asia Friedman, and Jeanne M. Ferrante. "Emotional consequences of persistently elevated PSA with negative prostate biopsies." *American Journal of Cancer Prevention* 1.1 (2013): 4-8.

27. Aubry, Wade, et al. "Budget impact model: epigenetic assay can help avoid unnecessary repeated prostate biopsies and reduce healthcare spending."*American health & drug benefits* 6.1 (2013).

28. Mariotto, Angela B., et al. "Projections of the cost of cancer care in the United States: 2010–2020." *Journal of the National Cancer Institute* (2011).

29. Graham J, Whelan P, Tewari A. Prostate Cancer : Diagnosis And Clinical Management [e-book]. Chichester, West Sussex, UK: Wiley-Blackwell; 2014. Available from: eBook Collection (EBSCOhost), Ipswich, MA

30. Tan CH, Wei W, Johnson V, Kundra V. Diffusion-Weighted MRI in the Detection of Prostate Cancer: Meta-Analysis. American Journal of Roentgenology. 2012;199(4):822-9.

31. Chavhan, Govind B., et al. "Principles, techniques, and applications of T2*-based MR imaging and its special applications 1." *Radiographics* 29.5 (2009): 1433-1449.

32. Hahn, Erwin L. "Spin echoes." *Physical review* 80.4 (1950): 580.

33. Stejskal, Edward O., and John E. Tanner. "Spin diffusion measurements: spin echoes in the presence of a time-dependent field gradient." *The journal of chemical physics* 42.1 (1965): 288-292.

34. Tanner, John E., and Edward O. Stejskal. "Restricted self-diffusion of protons in colloidal systems by the pulsed-gradient, spin-echo method." *The Journal of Chemical Physics* 49.4 (1968): 1768-1777.

35. de Rooij, Maarten, et al. "Accuracy of multiparametric MRI for prostate cancer detection: a meta-analysis." *American Journal of Roentgenology*202.2 (2014): 343-351.

36. Delongchamps, Nicolas Barry, et al. "Multiparametric MRI is helpful to predict tumor focality, stage, and size in patients diagnosed with unilateral low-risk prostate cancer." *Prostate cancer and prostatic diseases* 14.3 (2011): 232-237.

37. Sadinski, Meredith, et al. "Short-term reproducibility of apparent diffusion coefficient estimated from diffusion-weighted MRI of the prostate."*Abdominal imaging* 40.7 (2015): 2523-2528.

38. Sadinski, M., Karczmar, G., Peng, Y., Wang, S., Jiang, Y., Medved, M., Yousuf, A., Antic, T. and Oto, A. Pilot study of the use of hybrid multidimensional T2-DW-MRI for diagnosis of Pca and evaluation of Gleason score, American Journal of Roentgenology (in press).

39. Haider MA, van der Kwast TH, Tanguay J, et al. Combined T2-weighted and diffusion-weighted MRI for localization of prostate cancer. American Journal of Roentgenology. 2007;189(2):323-8.

40. Kajihara H, Hayashida Y, Murakami R, et al. Usefulness of Diffusion-Weighted Imaging in the Localization of Prostate Cancer. Int J Radiat Oncol Biol Phys. 2009;74(2):399-403.

41. Oto A, Yang C, Kayhan A, et al. Diffusion-Weighted and Dynamic Contrast-Enhanced MRI of Prostate Cancer: Correlation of Quantitative MR Parameters With Gleason Score and Tumor Angiogenesis. American Journal of Roentgenology. 2011;197(6):1382-90.

42. Rosenkrantz AB, Mannelli L, Kong XT, et al. Prostate Cancer: Utility of Fusion of T2-Weighted and High b-Value Diffusion-Weighted Images for Peripheral Zone Tumor Detection and Localization. Journal of Magnetic Resonance Imaging. 2011;34(1):95-100.

43. Lim HK, Kim JK, Kim KA, Cho K-S. Prostate Cancer: Apparent Diffusion Coefficient Map with T2-weighted Images for Detection-A Multireader Study. Radiology. 2009;250(1):145-51.

44. Woodfield CA, Tung GA, Grand DJ, Pezzullo JA, Machan JT, Renzulli JF, II. Diffusion-Weighted MRI of Peripheral Zone Prostate Cancer: Comparison of Tumor Apparent Diffusion Coefficient With Gleason Score and Percentage of Tumor on Core Biopsy. American Journal of Roentgenology. 2010;194(4):W316-W22.

45. Kitajima K, Kaji Y, Fukabori Y, Yoshida K-i, Suganuma N, Sugimura K. Prostate Cancer Detection With 3 T MRI: Comparison of Diffusion-Weighted Imaging and Dynamic Contrast-Enhanced MRI in Combination With T2-Weighted Imaging. Journal of Magnetic Resonance Imaging. 2010;31(3):625-31.

46. Mehta R, Kyshtoobayeva A, Kurosaki T, et al. Independent association of angiogenesis index with outcome in prostate cancer. Clinical Cancer Research. 2001;7(1):81-8.

47. Hosseinzadeh K, Schwarz SD. Endorectal diffusion-weighted imaging in prostate cancer to differentiate malignant and benign peripheral zone tissue. Journal of Magnetic Resonance Imaging. 2004;20(4):654-61.

48. Hötker, Andreas M., et al. "Prostate Cancer: assessing the effects of androgen-deprivation therapy using quantitative diffusion-weighted and dynamic contrast-enhanced MRI." *European radiology* 25.9 (2015): 2665-2672.

49. Padhani AR, Liu G, Chenevert TL, et al. Diffusion-Weighted Magnetic Resonance Imaging as a Cancer Biomarker: Consensus and Recommendations. Neoplasia. 2009;11(2):102-25.

50. Clarke LP, Croft BS, Nordstrom R, Zhang H, Kelloff G, Tatum J. Quantitative Imaging for Evaluation of Response to Cancer Therapy. Translational Oncology. 2009;2(4):195-7.

51. Sasaki M, Yamada K, Watanabe Y, et al. Variability in Absolute Apparent Diffusion Coefficient Values across Different Platforms May Be Substantial: A Multivendor, Multi-institutional Comparison Study. Radiology. 2008;249(2):624-30.

52. Sharp GC, Kandasamy N, Singh H, Folkert M. GPU-based streaming architectures for fast cone-beam CT image reconstruction and demons deformable registration. Physics in Medicine and Biology. 2007;52(19):5771-83.

53. Chenevert TL, Galban CJ, Ivancevic MK, et al. Diffusion Coefficient Measurement Using a Temperature-Controlled Fluid for Quality Control in Multicenter Studies. Journal of Magnetic Resonance Imaging. 2011;34(4):983-7.

54. Malyarenko D, Galban CJ, Londy FJ, et al. Multi-system Repeatability and Reproducibility of Apparent Diffusion Coefficient Measurement Using an Ice-Water Phantom. Journal of Magnetic Resonance Imaging. 2012;37(5):1238-46.

55. Braithwaite AC, Dale BM, Boll DT, Merkle EM. Short- and Midterm Reproducibility of Apparent Diffusion Coefficient Measurements at 3.0-T Diffusion-weighted Imaging of the Abdomen. Radiology. 2009;250(2):459-65.

56. Kim SY, Lee SS, Byun JH, et al. Malignant Hepatic Tumors: Short-term Reproducibility of Apparent Diffusion Coefficients with Breath-hold and Respiratory-triggered Diffusion-weighted MR Imaging. Radiology. 2010;255(3):815-23.

57. Litjens GJS, Hambrock T, Hulsbergen-van de Kaa C, Barentsz JO, Huisman HJ. Interpatient Variation in Normal Peripheral Zone Apparent Diffusion Coefficient: Effect on the Prediction of Prostate Cancer Aggressiveness. Radiology. 2012;265(1):260-6.

58. Gibbs P, Pickles MD, Turnbull LW. Repeatability of echo-planar-based diffusion measurements of the human prostate at 3 T. Magn Reson Imaging. 2007;25(10):1423-9.

59. Akin O, Gultekin DH, Vargas HA, et al. Incremental value of diffusion weighted and dynamic contrast enhanced MRI in the detection of locally recurrent prostate cancer after radiation treatment: preliminary results. *Eur Radiol*. 2011;21(9):1970-8.

60. Bittencourt LK, Barentsz JO, Duarte de Miranda LC, Gasparetto EL. Prostate MRI: diffusion-weighted imaging at 1.5T correlates better with prostatectomy Gleason grades than TRUS-guided biopsies in peripheral zone tumours. *Eur Radiol*. 2012;22(2):468-75.

61. Fuchsjager M, Akin O, Shukla-Dave A, Pucar D, Hricak H. The role of MRI and MRSI in diagnosis, treatment selection, and post-treatment follow-up for prostate cancer. Clinical advances in hematology & oncology : H&O. 2009;7(3):193-202.

62. Mazaheri Y, Shukla-Dave A, Muellner A, Hricak H. MRI of the Prostate: Clinical Relevance and Emerging Applications. *J Magn Reson Imaging*. 2011;33(2):258-74.

63. Turkbey B, Choyke PL. Multiparametric MRI and prostate cancer diagnosis and risk stratification. *Cur Opin Urol*. 2012;22(4):310-5.

64. Vargas HA, Akin O, Franiel T, et al. Diffusion-weighted Endorectal MR Imaging at 3 T for Prostate Cancer: Tumor Detection and Assessment of Aggressiveness. *Radiology*. 2011;259(3):775-84.

65. Yakar D, Debats OA, Bomers JGR, et al. Predictive value of MRI in the localization, staging, volume estimation, assessment of aggressiveness, and guidance of radiotherapy and biopsies in prostate cancer. *J Magn Reson Imaging*. 2012;35(1):20-31.

66. Gibbs P, Liney GP, Pickles MD, Zelhof B, Rodrigues G, Turnbull LW. Correlation of ADC and T2 Measurements With Cell Density in Prostate Cancer at 3.0 Tesla. *Invest Radiol.* 2009;44(9):572-6.

67. Soylu FN, Peng Y, Jiang Y, et al. Seminal Vesicle Invasion in Prostate Cancer: Evaluation by Using Multiparametric Endorectal MR Imaging. *Radiology*. 2013;267(3):797-806.

68. Wu L-M, Xu J-R, Ye Y-Q, Lu Q, Hu J-N. The Clinical Value of Diffusion-Weighted Imaging in Combination With T2-Weighted Imaging in Diagnosing Prostate Carcinoma: A Systematic Review and Meta-Analysis. *Am J Roent*. 2012;199(1):103-10.

69. Ababneh Z, Beloeil H, Berde CB, Gambarota G, Maier SE, Mulkern RV. Biexponential parameterization of diffusion and T-2 relaxation decay curves in a rat muscle edema model: Decay curve components and water compartments. *Magn Reson Med*. 2005;54(3):524-31.

70. Burdette JH, Elster AD, Ricci PE. Acute cerebral infarction: Quantification of spin-density and T2 shine-through phenomena on diffusion-weighted MR images. *Radiology*. 1999;212(2):333-9.

71. Maedler B, Drabycz SA, Kolind SH, Whittall KP, MacKay AL. Is diffusion anisotropy an accurate monitor of myelination? Correlation of multicomponent T-2 relaxation and diffusion tensor anisotropy in human brain. *Magn Reson Imaging*. 2008;26(7):874-88.

72. Stanisz GJ, Henkelman RM. Diffusional anisotropy of T-2 components in bovine optic nerve. *Magn Reson Med*. 1998;40(3):405-10.

73. Does MD, Gore JC. Compartmental study of diffusion and relaxation measured in vivo in normal and ischemic rat brain and trigeminal nerve. *Magn Reson Med*. 2000;43(6):837-44.

74. Wang S, Peng Y, Medved M, et al. Hybrid multidimensional T2 and diffusion-weighted MRI for prostate cancer detection. J. Magn. Reson. Imaging, 2014;39:781–788.

75. Metz CE. ROC software. http://metz-roc.uchicago.edu/.

76. Fan X, Haney CR, Agrawal G, et al. High-Resolution MRI of Excised Human Prostate Specimens Acquired with 9.4T in Detection and Identification of Cancers: Validation of a Technique. *J Magn Reson Imaging*. 2011;34(4):956-61.

77. Peng Y, Jiang Y, Eisengart L, Healy M, Straus F, Yang X. Computer-aided identification of prostatic adenocarcinoma: Segmentation of glandular structures, 2011.

78. Tabesh A, Teverovskiy M, Pang H-Y, et al. Multifeature prostate cancer diagnosis and Gleason grading of histological images. *Ieee Trans Med Imaging*. 2007;26(10):1366-78.

79. Ling GN, Tucker M. NUCLEAR MAGNETIC-RESONANCE RELAXATION AND WATER CONTENTS IN NORMAL MOUSE AND RAT-TISSUES AND IN CANCER-CELLS. *J Natl Cancer Inst*. 1980;64(5):1199-207.

80. White NS, Dale AM. Distinct Effects of Nuclear Volume Fraction and Cell Diameter on High b-Value Diffusion MRI Contrast in Tumors. *Magn Reson Med*. 2014;72(5):1435-43.

81. Beall, Paula T., Carlton F. Hazlewood, and Potu N. Rao. "Nuclear magnetic resonance patterns of intracellular water as a function of HeLa cell cycle."*Science* 192.4242 (1976): 904-907.

82. Bottomley PA, Hardy CJ, Argersinger RE, Allenmoore G. A REVIEW OF H-1 NUCLEAR-MAGNETIC-RESONANCE RELAXATION IN PATHOLOGY - ARE T1 AND T2 DIAGNOSTIC. *Med Phys*. 1987;14(1):1-37.

83. Callahan, D. E., et al. "NMR studies of intracellular water at 300 MHz: T2-specific relaxation mechanisms in synchronized or EGF-stimulated cells."*Magnetic resonance in medicine* 22.1 (1991): 68-80.

84. De Certaines, J., et al. "Proton NMR variations of T 1 and T 2 relaxation times in non cancerous normal or pathologic liver." *Nuclear medicine and biology*. 1982.

85. Langer D, Kwast TH, Evans A, et al. Intermixed Normal Tissue within Prostate Cancer: Effect on MR Imaging Measurement of Apparent Diffusion Coefficient and T2-Sparse versus Dense Cancers. *Radiology*. 2008;249(3):900-8.

86. Aydin, Hasan, et al. "Detection of prostate cancer with magnetic resonance imaging: optimization of T1-weighted, T2-weighted, dynamic-enhanced T1-weighted, diffusion-weighted imaging apparent diffusion coefficient mapping sequences and MR spectroscopy, correlated with biopsy and histopathological findings." *Journal of computer assisted tomography* 36.1 (2012): 30-45.

87. Hötker, Andreas M., et al. "Assessment of Prostate Cancer Aggressiveness by Use of the Combination of Quantitative DWI and Dynamic Contrast-Enhanced MRI." *American Journal of Roentgenology* 206.4 (2016): 756-763.

88. Kanda, Tomonori, et al. "Gadolinium-based contrast agent accumulates in the brain even in subjects without severe renal dysfunction: evaluation of autopsy brain specimens with inductively coupled plasma mass spectroscopy." *Radiology* 276.1 (2015): 228-232.

89. Kanda, Tomonori, et al. "High signal intensity in dentate nucleus on unenhanced T1-weighted MR images: association with linear versus macrocyclic gadolinium chelate administration." *Radiology* 275.3 (2015): 803-809.

90. Darrah, Thomas H., et al. "Incorporation of excess gadolinium into human bone from medical contrast agents." *Metallomics* 1.6 (2009): 479-488.

91. McDonald, Robert J., et al. "Intracranial gadolinium deposition after contrast-enhanced MR imaging." *Radiology* 275.3 (2015): 772-782.

92. Deo, Aneet, Mitchell Fogel, and Shawn E. Cowper. "Nephrogenic systemic fibrosis: a population study examining the relationship of disease development to gadolinium exposure." *Clinical Journal of the American Society of Nephrology* 2.2 (2007): 264-267.

93. Kuo, Phillip H., et al. "Gadolinium-based MR contrast agents and nephrogenic systemic fibrosis 1." *Radiology* 242.3 (2007): 647-649.

94. High, Whitney A., et al. "Gadolinium is detectable within the tissue of patients with nephrogenic systemic fibrosis." *Journal of the American Academy of Dermatology* 56.1 (2007): 21-26.

95. Morcos, S. K. "Extracellular gadolinium contrast agents: differences in stability." *European journal of radiology* 66.2 (2008): 175-179.

96. Murata, Nozomu, et al. "Macrocyclic and Other Non-Group 1 Gadolinium Contrast Agents Deposit Low Levels of Gadolinium in Brain and Bone Tissue: Preliminary Results From 9 Patients With Normal Renal Function."*Investigative radiology* (2016).

97. van Niekerk, Cornelis G., et al. "Microvascularity in transition zone prostate tumors resembles normal prostatic tissue." *The Prostate* 73.5 (2013): 467-475.

98. Kershaw, Lucy E., Charles E. Hutchinson, and David L. Buckley. "Benign prostatic hyperplasia: Evaluation of T1, T2, and microvascular characteristics with T1-weighted dynamic contrast-enhanced MRI." *Journal of Magnetic Resonance Imaging* 29.3 (2009): 641-648.

99. Langer, Deanna L., et al. "Prostate tissue composition and MR measurements: investigating the relationships between ADC, T2, K trans, ve, and corresponding histologic features 1." *Radiology* 255.2 (2010): 485-494.

100. Storås, Tryggve H., et al. "Prostate magnetic resonance imaging: multiexponential T2 decay in prostate tissue." *Journal of Magnetic Resonance Imaging* 28.5 (2008): 1166-1172.

101. Kjaer, L., et al. "In vivo estimation of relaxation processes in benign hyperplasia and carcinoma of the prostate gland by magnetic resonance imaging." *Magnetic resonance imaging* 5.1 (1987): 23-30.

102. Chatterjee, A., Watson, G., Myint, E., Sved, P., McEntee, M., & Bourne, R. (2015). Changes in epithelium, stroma, and lumen space correlate more strongly with gleason pattern and are stronger predictors of prostate ADC changes than cellularity metrics1. *Radiology, 277*(3), 751-762. doi:10.1148/radiol.2015142414

103. Mustafi, D., et al. "IV Administered Gadodiamide Enters the Lumen of the Prostatic Glands: X-Ray Fluorescence Microscopy Examination of a Mouse Model." *AJR. American journal of roentgenology* 205.3 (2015): W313.

104. Peng, Y. et al. “Apparent Diffusion Coefficient for Prostate Cancer Imaging: Impact of b Values.” *AJR. American journal of roentgenology* 202.3, W247-W253

APPENDIX A

IMPLICATIONS OF A SPECIAL CASE OF B-VALUE CHOICE

Diffusion weighted imaging (DWI) has become an integral part of a standard multiparametric MRI prostate exam. Apparent diffusion coefficient (ADC) maps, derived from Diffusion weighted images, are not only evaluated qualitatively, but there is also increasing interest in quantitative evaluation of ADC. It has been established that choice of b value significantly affects ADC calculation (104). Ideally, several b values will be used to acquire diffusion weighted images. This may not be practical in certain situations, however, where time is limited and the DWI scan must be performed quickly. The use of two b values in conjunction with a b=0 s/mm^2 image is a common choice. It may be intuitive to choose these b values to be equally spaced for the most accurate estimate of ADC. In fact, the use of a least squares estimation algorithm in combination with this particular sampling scheme results in the omission of image data in the ADC calculation.

Let's say we use 2 b values where the second b value is 2 times the first b value. If we write the signal equation in matrix form denoting the first b value as "b" then we have

$$y = Ax$$

$$y = \begin{pmatrix} \log(S_0) \\ \log(S_b) \\ \log(S_{2b}) \end{pmatrix}, \qquad A = \begin{pmatrix} 1 & 0 \\ 1 & b \\ 1 & 2b \end{pmatrix}, \qquad x = \begin{pmatrix} y\ intercept \\ -ADC \end{pmatrix}$$

The least squares estimate of x is given by

$$\hat{x} = argmin(\|Ax - y\|_2^2)$$

The well-known solution to this problem is given by

$$\hat{x} = (A^T A)^{-1} A^T y$$

Performing the algebra, we can see that S_b has no influence on ADC:

$$(A^T A)^{-1} = \left[\begin{pmatrix} 1 & 1 & 1 \\ 0 & b & 2b \end{pmatrix} \begin{pmatrix} 1 & 0 \\ 1 & b \\ 1 & 2b \end{pmatrix} \right]^{-1}$$

$$(A^T A)^{-1} = \begin{pmatrix} 3 & 3b \\ 3b & 5b^2 \end{pmatrix}^{-1}$$

$$(A^T A)^{-1} = \frac{1}{6b^2} \begin{pmatrix} 5b^2 & -3b \\ -3b & 3 \end{pmatrix}$$

$$\hat{x} = \frac{1}{6b^2} \begin{pmatrix} 5b^2 & -3b \\ -3b & 3 \end{pmatrix} \begin{pmatrix} 1 & 1 & 1 \\ 0 & b & 2b \end{pmatrix} \begin{pmatrix} \log(S_0) \\ \log(S_b) \\ \log(S_{2b}) \end{pmatrix}$$

$$\hat{x} = \frac{1}{6b^2} \begin{pmatrix} 5b^2 & 2b^2 & -b^2 \\ -3b & 0 & 3b \end{pmatrix} \begin{pmatrix} \log(S_0) \\ \log(S_b) \\ \log(S_{2b}) \end{pmatrix}$$

$$\hat{x} = \frac{1}{6b^2} \begin{pmatrix} 5b^2 \cdot \log(S_0) + 2b^2 \cdot \log(S_b) - b^2 \cdot \log(S_{2b}) \\ -3b \cdot \log(S_0) + 3b \cdot \log(S_{2b}) \end{pmatrix}$$

$$intercept = \frac{5}{6}\log(S_0) + \frac{1}{3}\log(S_b) - \frac{1}{6}\log(S_{2b})$$

$$\boldsymbol{ADC = \frac{1}{2b}(\log(S_0) - \log(S_{2b}))}$$

The effect of this b-value sampling scheme on ADC of prostate cancer and normal prostatic tissue was assessed using the data set described in Chapter 3. Apparent diffusion coefficient (ADC) was calculated at both TEs and three subsets of b

values : 0 and 750 s/mm^2 ($ADC_{0,750}$), 0 and 1500 s/mm^2 ($ADC_{0,1500}$) and 750 and 1500 s/mm^2 ($D_{750,1500}$). In the final case, the b=0 data is omitted which gives the pure diffusion coefficient, D, as opposed to ADC which includes perfusion effects. The six diffusion coefficients were compared between cancer and normal ROIs using the two-sided, Mann Whitney U test and $ADC_{0,750}$, $ADC_{0,1500}$ and $D_{750,1500}$ were compared at each TE for normal and cancer ROIs using the Friedman test. A Bonferroni correction for 10 multiple comparisons was applied, setting the effective significance level at α=0.005.

All three methods of diffusion coefficient calculation yielded ADC significantly higher in normal ROIs than in cancer ROIs at both TEs. The difference in mean ADC between cancer and normal ROIs across all patients was greatest for $ADC_{0,750}$ with TE=75 ms (normal mean ± standard deviation 1.82 ± 0.4 mm^2/s, cancer 1.09 ± 0.4 mm^2/s). Tumor morphology and size did appear different on diffusion coefficient maps depending on b values used. $ADC_{0,750}$, $ADC_{0,1500}$ and $D_{750,1500}$ were significantly different from each other in normal and cancer ROIs at both TEs. Patient images are included at the end of this appendix.

Table A.1 Mean and standard deviation of as a function of TE and b-value across all patients. ADC/D calculations were all performed on a voxel-by-voxel basis. Results are reported in 10^{-3}mm^2/s.

	$ADC_{0,750}$	*$ADC_{0,1500}$*	*$D_{750,1500}$*
	TE=47 ms		
Normal	1.65 ± 0.3	1.32 ± 0.3	1.00 ± 0.2
Cancer	1.02 ± 0.3	0.83 ± 0.2	0.64 ± 0.2
	TE=75 ms		
Normal	1.82 ± 0.4	1.47 ± 0.3	1.12 ± 0.3
Cancer	1.09 ± 0.4	0.89 ± 0.3	0.68 ± 0.2

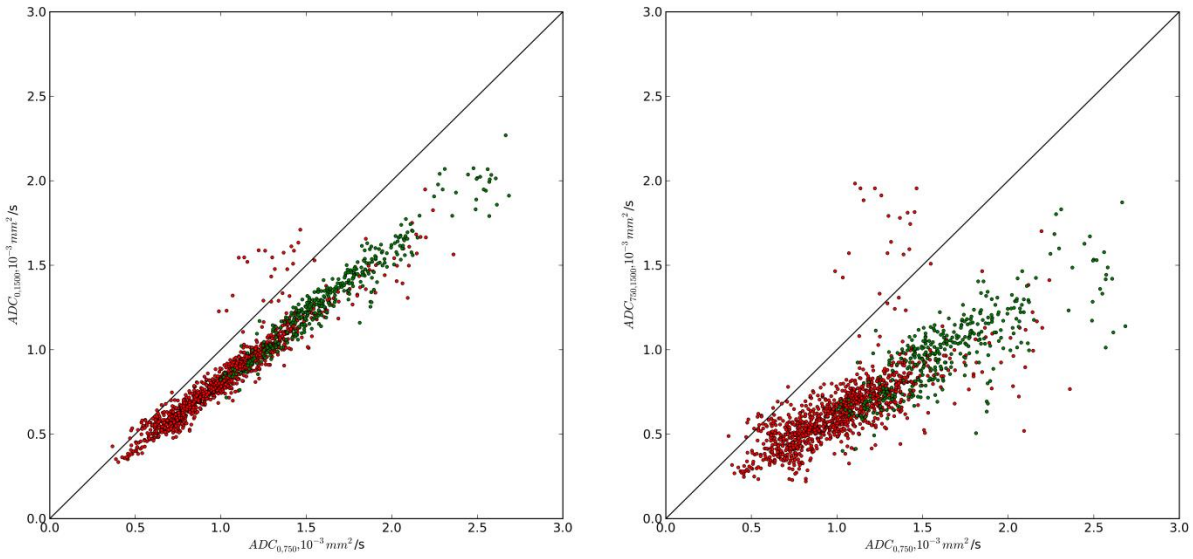

Figure A.1 $ADC_{0,1500}$ vs $ADC_{0,750}$ (left)and $D_{750,1500}$ vs $ADC_{0,750}$ (right)at TE= 47 ms. Red dots are cancer voxels and green dots are normal voxels.

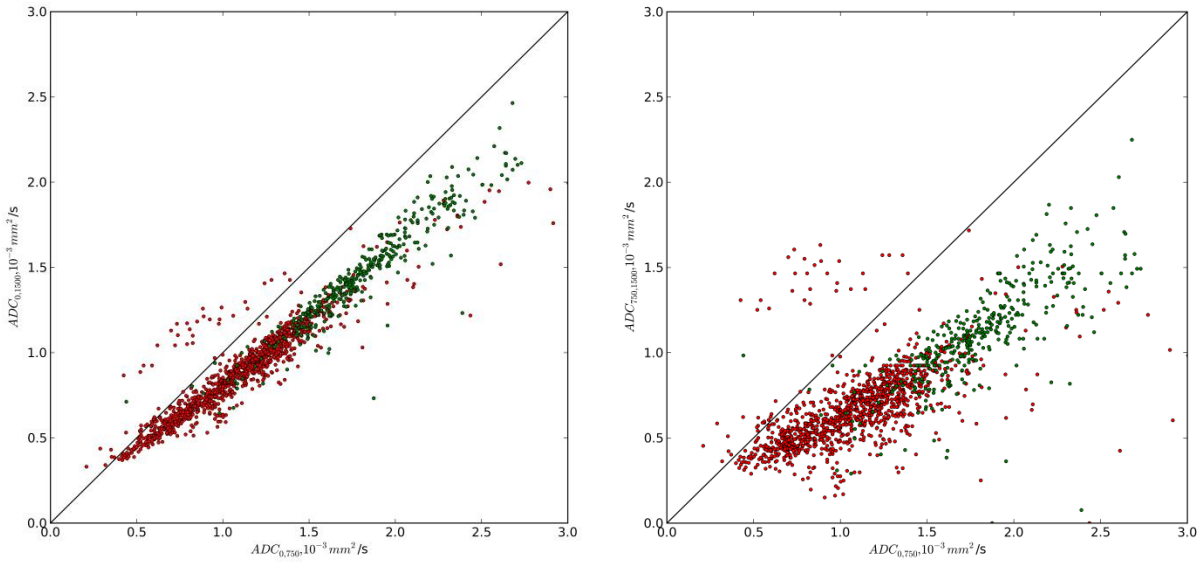

Figure A.2 $ADC_{0,1500}$ vs $ADC_{0,750}$ (left) and $D_{750,1500}$ vs $ADC_{0,750}$ (right) at TE= 75 ms. Red dots are cancer voxels and green dots are normal voxels.

The choice of b value significantly affects ADC calculation, which may be problematic for the development of ADC as an image-based biomarker. The analysis presented in this appendix shows that cancer and normal ADCs are significantly different in prostate no matter the choice of b values used, although b values of 0 and

750 s/mm^2 yielded greater separation between the two ROI types. The choice of b value is therefore unlikely to mar the qualitative evaluation of ADC maps. When evaluating ADC quantitatively, however, parameter choice becomes very important as simply changing one of two b values used can change mean ADC by up to 65%.

In prostate cancer, low ADC is likely the result of small glandular lumen volume and dense cellular growth with limited extracellular space. Epithelial cells growing into the ductal lumen restrict the number and size of lumen. The formation of crytstalloids in the lumen presents further barriers to diffusion. The luminal fluid also becomes more mucosal in cancerous tissue which should lower the diffusion constant. The reduction of extracellular space creates barriers to diffusion on a smaller scale. Additionally, cellular changes such as nucleomegaly and apoptosis change the tortuosity of different microenvironments and diffusivity and proportions of different compartments of water molecules within the cancerous tissue. The analysis presented here suggests that by using poorly chosen b values, ADC can become unknowingly insensitive to diffusion barriers on a shorter scale and could affect which mechanisms in cancer which are responsible for changes in measured ADC.

More than two b values should be used clinically, but for research scans when time may be very limited b value choice should be approached with caution. In particular, it is important not to choose b values of 0, b and 2b as the middle (b) acquisition affects only the perfusion fraction and not the ADC calculation.

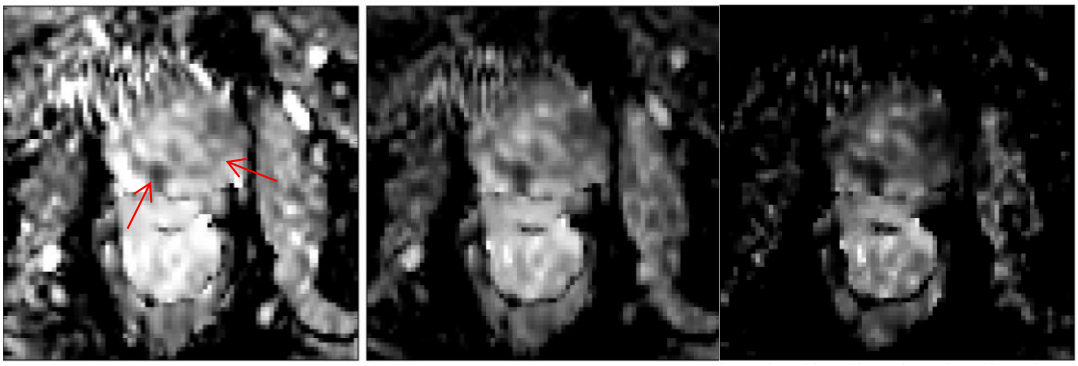

$ADC_{0,750}$ $ADC_{0,1500}$ $D_{750,1500}$

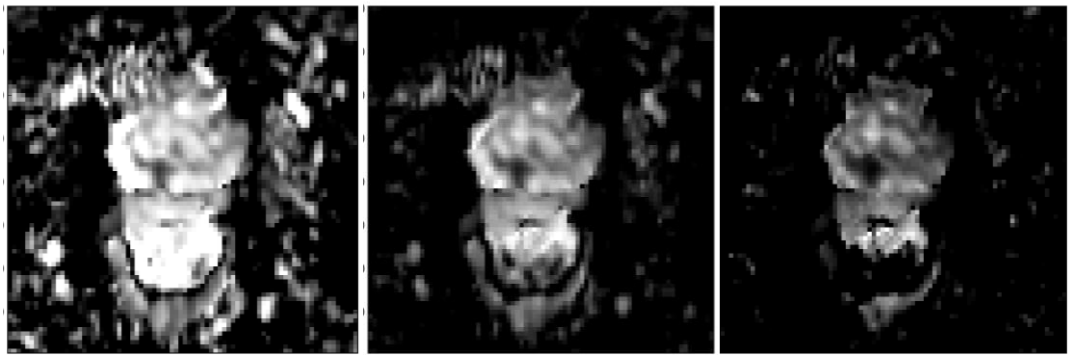

$ADC_{0,750}$ $ADC_{0,1500}$ $D_{750,1500}$

Figure A.3 Maps of the 3 calculated diffusion coefficients at TE=47 ms (upper row) and TE=75 ms (lower row) for a patient with two Gleason 7 cancer foci indicated by the red arrows. Window and level are constant across all images.

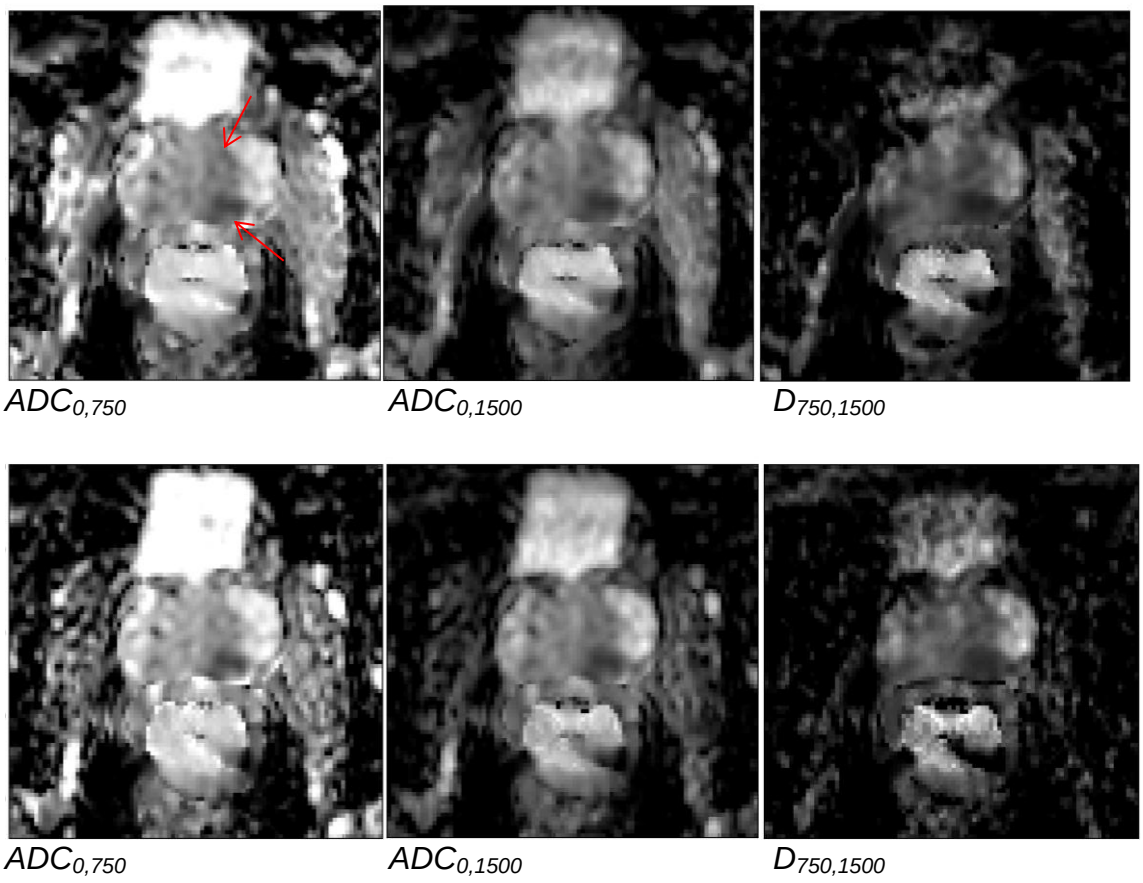

Figure A.4 Maps of the 3 calculated diffusion coefficients at TE=47 ms (upper row) and TE=75 ms (lower row) for a patient with a Gleason 7 cancer (lower red arrow) and BPH (upper red arrow). Window and level are constant across all images.